Nanoscale

REVIEW

View Article Online
View Journal | View Issue

Cite this: *Nanoscale*, 2022, **14**, 10268

Photocatalytic CO_2 conversion: from C1 products to multi-carbon oxygenates

Quan Zhang, Chao Yang, Anxiang Guan, Miao Kan and Gengfeng Zheng *

Received 11th May 2022,
Accepted 4th July 2022

DOI: 10.1039/d2nr02588d

rsc.li/nanoscale

Photocatalytic CO_2 conversion into high-value chemicals has been emerging as an attractive research direction in achieving carbon resource sustainability. The chemical products can be categorized into C1 and multi-carbon (C_{2+}) products. In this review, we describe the recent research progress in photocatalytic CO_2 conversion systems from C1 products to multi-carbon oxygenates, and analyze the reasons related to their catalytic mechanisms, as the production of multi-carbon oxygenates is generally more difficult than that of C1 products. Then we discuss several examples in promoting the photoconversion of CO_2 to value-added multi-carbon products in the aspects of photocatalyst design, mass transfer control, determination of active sites, and intermediate regulation. Finally, we summarize perspectives on the challenges and propose potential directions in this fast-developing field, such as the prospect of CO_2 transformation to long-chain hydrocarbons like salicylic acid or even plastics.

1. Introduction

The concentration of atmospheric carbon dioxide (CO_2) has been continuously increasing from its pre-industrial level over the past several decades.[1,2] The National Oceanic and Atmospheric Administration in the United States announced in early 2022 that the monitored daily average concentration of CO_2 has reached over 410 ppm.[3] New technologies for CO_2 capture, storage and conversion have been widely investigated with efforts from both industrial and scientific communities.[4–6]

Photocatalytic CO_2 conversion represents a unique and highly potential approach to boost the CO_2 conversion for achieving carbon neutrality and energy sustainability, due to its clean and selective reaction characteristics.[7,8] At present, the photocatalytic CO_2 conversion products can be roughly categorized into C1 and multi-carbon (C_{2+}) products, based on the number of derived carbon atoms in the molecular formulas. With substantial research progress to date, the photocatalytic conversion of CO_2 into C1 molecules, including carbon monoxide (CO), methane (CH_4), and methanol (CH_3OH), has been widely reported.[9,10] On the other hand, the obtaining of C_{2+} products, especially oxygenates such as ethanol and acetic acid, is still confronting great challenges due to the complex steps and competitive reaction pathways in photocatalytic CO_2 conversion reactions.[11,12] Although both C1 and C_{2+} products are originated from CO_2 and water, the C_{2+} products consume more CO_2 molecules and store higher energy in the molecules. Some C_{2+} products are also important raw materials for making chemicals with less energy waste, such as fuel additives, disinfectants and pharmaceuticals,[13,14] contributing to the efficient utilization of energy. Thus, from the perspective of both resource deployment and energy utilization, the direct transformation from abundant CO_2 to multi-carbon oxygenates not only facilitates the carbon neutralization process, but more importantly, allows to generate higher value-added compounds for chemical industry and daily life resources.

Promoting CO_2 photoreduction to C_{2+} products, therefore, has been a hot topic. Albero *et al.* summarized the formation of compounds of two or more carbon atoms in the photocatalytic CO_2 reduction to show how the product selectivity can be controlled, while less focus was made on explaining the challenges of producing C_{2+} products.[15] The pathways in photoreduction CO_2 to diverse products also deserve strong attention, because reactive sites in different pathways can have varied affinities to reactants, intermediates, and photoreduction products. Qiao and coauthors highlighted the promoted effects of atomic-level reactive sites in CO_2 photoreduction and outlined the design of photocatalysts with these reactive sites for in-depth understanding reactions pathways.[16] These are two major subjects in tuning product selectivity and reaction pathways. However, to date, the systematic comparison between the characteristics of photocatalytic CO_2 reduction systems and obtained diverse products is quite limited, especially for C1 products and C_{2+} oxygenates. Moreover, the reasons why the critical C–C coupling behavior for making C_{2+}

Laboratory of Advanced Materials, Department of Chemistry and Shanghai Key Laboratory of Molecular Catalysis and Innovative Materials, Faculty of Chemistry and Materials Science, Fudan University, Shanghai 200438, China.
E-mail: gfzheng@fudan.edu.cn

oxygenates occurs with less priority than C1 products have not been comprehensively analyzed. The mechanisms on reaction pathways of different photocatalysts and products should be carefully evaluated for understanding the photocatalytic conversion of CO_2 from C1 products to C_{2+} oxygenates.

Herein, this review systematically describes the research progress of photocatalytic CO_2 conversion from C1 to C_{2+} products, and demonstrate the mechanism that CO_2 molecules are relatively efficient to be converted into C1 products, but not C_{2+} oxygenates. The key C–C coupling process affected by CO_2 adsorption, intermediate formation and coupling reactions is focused. Aiming at the drawbacks in achieving CO_2 to C_{2+} oxygenates, we discuss some suggestions in the aspects of photocatalyst design, mass transfer control, determination of active sites, and intermediate regulation in the photocatalytic CO_2 conversion process. Finally, we summarize the challenges for converting CO_2 into both C1 products and C_{2+} oxygenates, as well as propose perspectives of direct conversion from CO_2 to value-added hydrocarbons with longer carbon chains, such as salicylic acid or even plastics.

2. Principle of photocatalytic CO_2 conversion

The typical process of photocatalytic CO_2 reduction on semiconductor photocatalysts mainly consists of four steps: light absorption, charge separation, CO_2 adsorption, and redox reactions.[17,18] The first step of a photocatalyst is to absorb photons from sunlight to produce electrons and holes on the conduction band (CB) and valence band (VB), respectively, which serve as reductant and oxidant in photocatalytic reactions. In order to reduce CO_2 molecules, the suitable band structure of photocatalysts is strictly demanded. Generally, the CB of the semiconductor must be more negative than the potential of CO_2 reduction, and the VB position must be positive than the potential of water oxidation (Fig. 1a). The second step is the spatial separation of photogenerated electron–hole pairs, while the reversible process as charge recombination can also take place. To increase charge separation efficiency and inhibit the charge recombination, the structural factors of photocatalysts that are closely related to the charger lifetime and transfer rate should be rationally tuned, including crystallinity, size, doping, and surface properties.[19–21] The third step is the CO_2 adsorption, which is the prerequisite for transferring electrons from the photocatalyst to CO_2 molecules or intermediates for triggering subsequent reduction reactions. In most of the reported works, the photocatalysts with higher surface area tend to provide more active sites for CO_2 adsorption.[22,23] Another useful way to improve CO_2 adsorption is the modification of alkali ions on the photocatalyst surface.[24] Due to its Lewis acidity of CO_2 molecules, the interaction between CO_2 and surface alkaline can significantly benefit the formation of active intermediates, such as bidentate carbonate, facilitating the participation in reduction reactions. The fourth step is the surface redox reactions with multiple parallel pathways and side reactions, as the most critical and complex step in photocatalytic CO_2 conversion.[25,26] Within this step, different kinds of CO_2 reduction products may be obtained depending on the reduction pathways, in which electrons are transferred from the photocatalyst surface to the adsorbates and/or solutions. The fourth step process is in principle similar to an electrochemical reduction. The standard reduction potentials and the required bandgap positions of several typical semiconductors for satisfying CO_2 reduction are illustrated (Fig. 1b), while the introduction of cocatalyst is also critical to further improve the overall CO_2 conversion efficiency in this key step.[27]

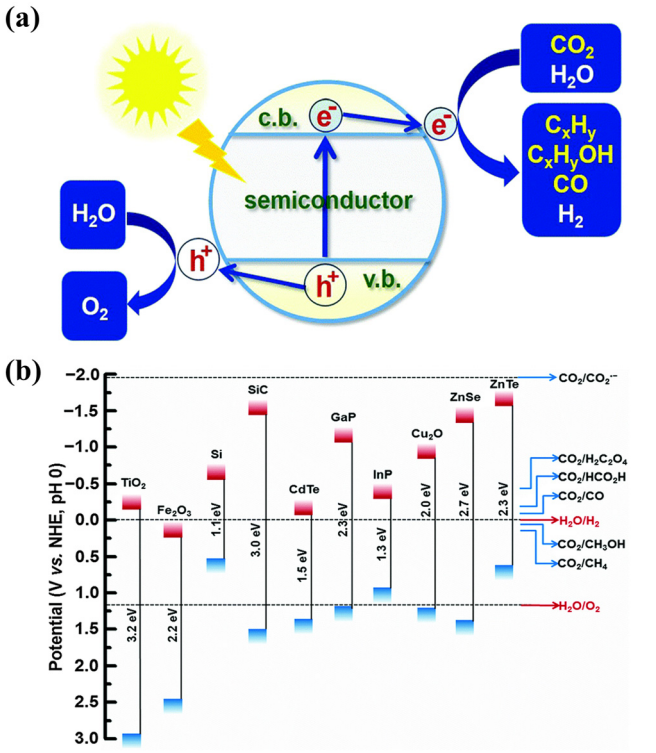

Fig. 1 (a) Principle of photocatalytic CO_2 conversion in terms of light absorption, charge separation, CO_2 adsorption and redox reactions.[28] Copyright 2020, Royal Society of Chemistry. (b) The standard reduction potentials and required band-gap positions of some typical semiconductors for satisfying CO_2 reduction reactions.[29] Copyright 2016, Royal Society of Chemistry.

3. Photocatalytic CO_2 conversion with different selectivities

Though the reduction products all come from simple CO_2 molecules, the photocatalytic CO_2 conversion process is complicated as it includes many multi-step reactions. Based on the number of carbon atoms in the obtained products, CO_2 can be generally converted into two categories of C1 and C_{2+} products. The C1 products include carbon monoxide (CO), methane (CH_4), formic acid (HCOOH), and methanol (CH_3OH), and the

C_{2+} products primarily consist of ethylene (C_2H_4), ethane (C_2H_6), acetaldehyde (CH_3CHO), ethanol (C_2H_5OH), acetic acid (CH_3COOH), and other C_{2+} products. In this section, we aim to summarize the current advances of C1 products and C_{2+} oxygenates, and discuss our understandings on the reasons that the C_{2+} oxygenates are more difficult to obtain than the C1 products.

3.1 Status of photocatalytic CO_2 conversion to C1 products

Generally, the hydrogenation steps are preferable for the production of C1 products in photocatalytic CO_2 reaction, and the required numbers of electrons and protons involving in reaction pathways are usually less than or equal to 8. Although the selectivity of C1 products varies from different specific reaction conditions, the conversion of CO_2 molecules toward C1 products is generally efficient.[30] For example, Li *et al.* prepared a bioinspired photocatalyst with flexible dual-metal-site pairs (DMSPs), which exhibited dynamic self-adaptive behavior to fit mutative C1 intermediates (Fig. 2a).[31] The Cu and Ni DMSPs were incorporated into a metal–organic framework (MOF) to prepare a MOF-808-CuNi catalyst, resulting in a high production rate of 158.7 μmol g^{-1} h^{-1} in the photocatalytic CO_2 conversion to CH_4, with a selectivity of 99.4% (electron basis) and 97.5% (product basis). In this work, the creation of an "adaptive" catalytic process of DMSPs to stabilize C1 intermediates improves the selectivity of CH_4 in a flexible microenvironment, suggesting the possibility of stabilizing reaction intermediates *via* the self-adaptive DMSP mechanism.

In addition to the catalytic system led by photocatalysts to promote the conversion of CO_2 to C1 products, the combination of photocatalysts with biological function has also emerged in photocatalytic CO_2 reduction reactions. For instance, Chen *et al.* reported a semi-artificial photosynthesis system by a cell engineering strategy.[32] In this process, CO_2 was consumed by wrapping halophilic bacteria membrane-derived vesicles on hollow porous TiO_2 nanoparticles deposited with Pd nanoparticle cocatalysts. In this bio-inorganic assembly system, the membrane protein bacteriorhodopsin not only retained its natural biological function of pumping protons, but also acted as a photosensitizer to inject photogenerated electrons into the conduction band of TiO_2. Therefore, both the electrons accumulated on the Pd cocatalyst and the protons gathered in the cell structure boosted the proton-coupled multi-electron transfer process for photocatalytic CO_2 conversion to CH_4 and CO. The formation of CH_4 and CO over the bio-inorganic assembly system, and the mass spectra of $^{13}CH_4$ and ^{13}CO products were further verified in $^{13}CO_2$ atmosphere (Fig. 2b and c).

The hot single-atom catalysis can also be utilized to promote the photocatalytic reduction of CO_2 to C1 products. Xiong *et al.* reported that the isolated Ni single atoms dispersed on defect-rich zirconia (Ni-SA-*x*/ZrO_2) showed an excellent yield rate (11.8 μmol g^{-1} h^{-1}) and selectivity (92.5%) toward CO production in the absence of sacrificial agents or sensitizers under Xe lamp irradiation (Fig. 2d).[33] Both the experimental and theoretical investigations proved that the lower energy barrier for the CO_2 to CO conversion was favorable *via* an adsorbed COOH intermediate on the atomically dispersed Ni sites, while the competing side reaction such as hydrogen evolution reaction should also be reduced. In the aspects of the methanol production, Wu *et al.* directly observed that the (110) facet of single Cu_2O particles were photo-catalytically more active for reducing CO_2 to methanol than the inert (100) facet by using correlated scanning fluorescence X-ray microscopy and environmental transmission electron microscopy at atmospheric pressure (Fig. 2e and f).[34] They also found that the oxidation state of the active sites changed from Cu(I) to Cu(II) due to the co-adsorption of CO_2 and H_2O and then changed back to Cu(I) after the CO_2 conversion under visible light illumination.

The plasmonic heterostructure was also introduced to boost photocatalytic CO_2 reduction to C1 products. For example, Jun *et al.* reported a ruthenium (Ru)-based asymmetric catalyst that was immobilized onto a plasmonic Au/TiO_2 heterostructure to efficiently and selectively convert CO_2 into formic acid in an aqueous solution.[35] The plasmonic heterostructure benefited the multi-electron transfer to facilitate CO_2 reduction through efficient charge separation at a Schottky junction (Fig. 2g). As a result, the photocatalyst exhibited a high turnover frequency of 1200 h^{-1} at 360 mW cm^{-2}, a superior selectivity towards formic acid (~95%) even at a low pH (~3), and a remarkable reusability over 50 hours without obvious loss of the catalytic activity. The widely used plasmonic effect is recognized as an effective means for improving photocatalytic CO_2 reaction into C1 products, but the size distribution, crystallinity and surface defects should be rationally designed when coupling with semiconductors.

Last but not least, the application of photovoltaic cells is an important direction for photocatalytic CO_2 conversion to C1 compounds.[36] Typically, an artificial photosynthetic system consisting of a photoanodic semiconductor that harvests solar photons to split H_2O and a cathodic catalyst for achieving the CO_2 reduction is required. Using this strategy (Fig. 2h),[37] a solar-to-syngas energy conversion efficiency of up to 13.6% was obtained, with a turnover frequency of 529.5 h^{-1} for highly stable CO production from CO_2, and a high Faradaic efficiency above 80%. Another work by the same group realized a CO-evolution rate of 265.3 mmol g^{-1} h^{-1} by integrating single-atom metal–insulator–semiconductor as the photoanode and a single-atom Ni-doped graphene as the cathode for efficient CO_2-to-syngas conversion (Fig. 2i).[38] The overall quantum efficiency of 5.7% was also recorded under 450 nm light irradiation with this artificial photosynthetic cell.

The aforementioned works provide examples for converting CO_2 into C1 products by photocatalysts or photovoltaic cells. In particular, the single-atom catalysts only contribute two electrons for CO production, due to the limitation of storing sufficient electrons in single atomic sties. Here, a brief summary of the representative works in photocatalytic CO_2 reduction to different C1 products is shown (Table 1). Except for formaldehyde, the almost 100% selectivity of these C1 products can be obtained by photocatalysis under light irradiation. For formaldehyde, the hydroxyl radicals ($^{\bullet}OH$) or

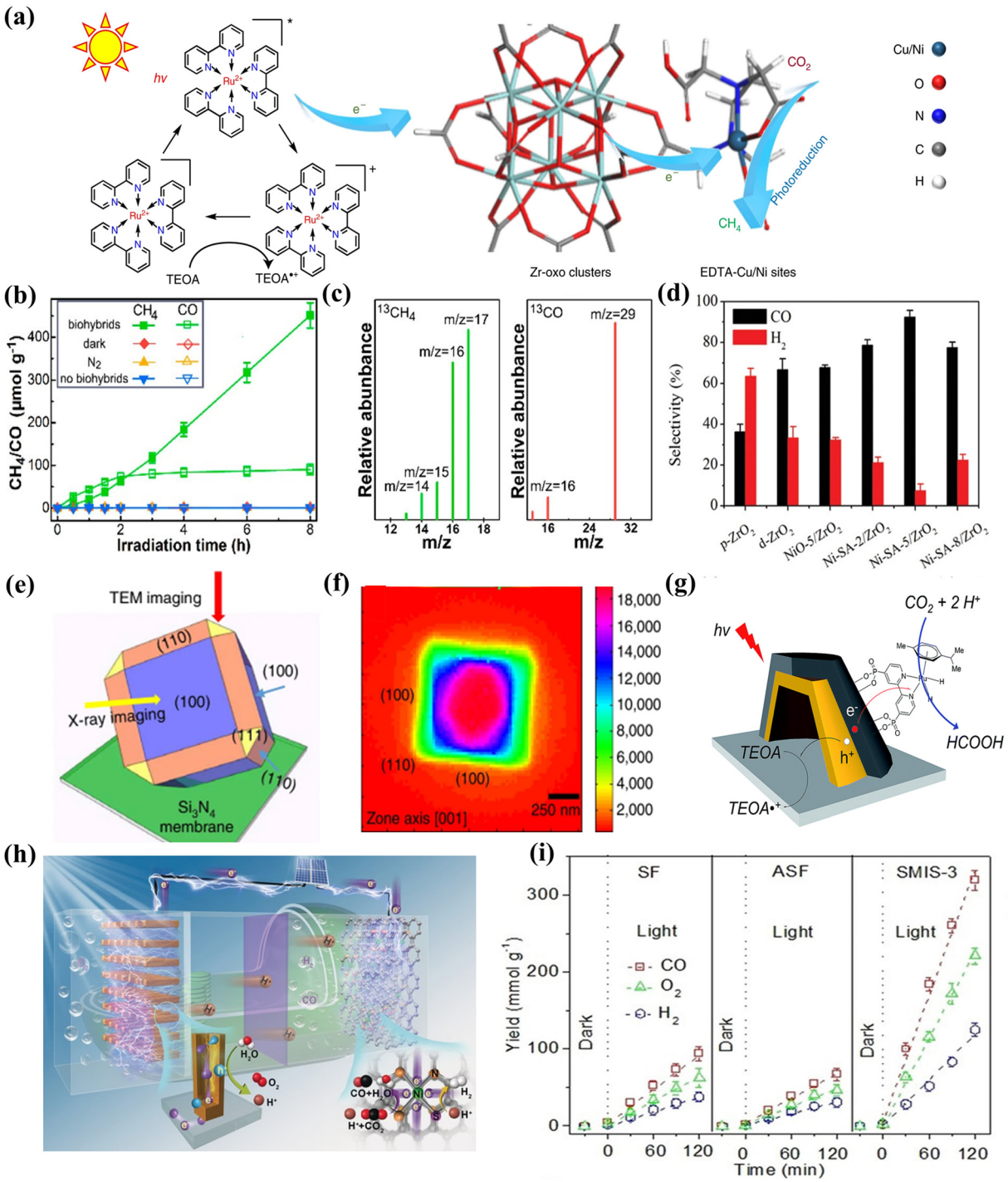

Fig. 2 (a) Schematic illustration of charge transfer in the photocatalytic CO_2 reaction with MOF-808-CuNi using $[Ru(bpy)_3]Cl_2{\cdot}6H_2O$ as a photosensitizer.[31] Copyright 2021, Springer Nature. (b) Photocatalytic CH_4 and CO formation over the bio-inorganic assembly system and (c) mass spectra of produced $^{13}CH_4$ and ^{13}CO over biohybrids in $^{13}CO_2$ atmosphere.[32] Copyright 2019, American Chemical Society. (d) H_2 and CO selectivity at reaction time of 5 h over different samples.[33] Copyright 2020, Wiley-VCH. (e) Schematic of the electron beam and X-ray directions for transmission electron microscopy (TEM) and scanning fluorescence X-ray microscopy (SFXM) imaging and (f) high-resolution SFXM image from Cu Kα emission with the incident X-ray beam parallel to the [001] direction.[34] The color scales indicate the intensity of the Cu fluorescence signal. Copyright 2019, Springer Nature. (g) Illustrations of the plasmonic photocatalyst heterostructure for production of formic acid.[35] Copyright 2019, Royal Society of Chemistry. (h) Model and mechanism of the photovoltaic-coupled two-compartment artificial photosynthetic cell for syngas production.[37] Copyright 2019, Wiley-VCH. (i) Time course for the formation of gaseous products in the different cells at 2.4 V.[38] Copyright 2021, Wiley-VCH.

Table 1 Summary of representative works toward photocatalytic conversion of CO_2 into C1 products

Photocatalysts	Products and selectivity	Reaction conditions	Ref.
Poly(3,4-ethylenedioxythiophene)	100% CO	Xe lamp, 250–950 nm	41
$CuIn_5S_8$ layers	100% CH_4	Xe lamp, ~50 mW cm^{-2}	42
Carbon nitride-like polymer/carbon dots	100% CH_3OH	300 W Xe lamp	43
Cd/ZnS:Cu	99% HCOOH	Solar light irradiation	44
$Ba_3Li_2Ti_8O_{20}$	50 μmol g^{-1} h^{-1} HCHO	20 W halogen lamp	45

superoxide radicals ($^{\bullet}O_2^-$) that are generated in photocatalytic reactions prefer to degrade formaldehyde rather than production. Indeed, the photocatalytic oxidation technology is often used for the mineralization of formaldehyde pollutants.[39,40] Thus, formaldehyde is generally not the main product in photocatalytic CO_2 reduction reactions.

3.2 Photocatalytic CO_2 conversion to multi-carbon products

Considering the higher values of multi-carbon oxygenates compared to the C1 products, increasing efforts have been directed for tuning the product selectivity toward C_{2+} oxygenates by photocatalysis. In this section, we will focus on the studies on multi-carbon products in photocatalytic CO_2 reduction reactions.

3.2.1 CO_2 molecule as individual reactants. Several promising approaches have been adopted to control the selectivity of C_{2+} products from individual CO_2 molecules. For example, Li *et al.* reported that the doping of a small amount (0.02%) of Co in a Cu/TiO_2 catalyst improved the selectivity of alkanes, making C_2H_6 as the main product and producing a small amount of C_3H_8 (Fig. 3a and b).[46] In their proposed mechanism, CO_2 first combined with e^- to form $^{\bullet}CO_2^-$, and was further reduced to CO through the HCO_3^- or CO_3^{2-} pathways. Then CO continued to react with multiple electrons and protons to form various hydrocarbon free radicals ($^{\bullet}CH$, $^{\bullet}CH_2$, $^{\bullet}CH_3$), and finally generated various hydrocarbons including CO, CH_4, C_2H_6 and C_3H_8 (Fig. 3c). The fabrication of bimetallic catalytic sites has been investigated for catalyzing C_{2+} olefin products. For instance, a $Cu^{\delta+}/CeO_2$–TiO_2 photocatalyst containing atomically dispersed $Cu^{\delta+}$ sites that were anchored on a CeO_2–TiO_2 heterostructure was constructed by the pyrolytic transformation of Cu^{2+}–Ce^{3+}/MIL-125-NH_2 precursors.[47] Under simulated sunlight irradiation, this photocatalyst exhibited a production rate of 4.51 μmol g^{-1} h^{-1} and 73.9% selectivity in terms of electron utilization for conversion of CO_2 to C_2H_4 on bimetallic Cu–Ce reactive sites (Fig. 3d).

Apart from the basic alkane and olefin products, C_{2+} oxygenates are other considerable products in CO_2 photoreduction reactions. For instance, a pyrolyzed cobalt-type zeolitic imidazolate framework (ZIF-67), namely ZIF-derived carbon (ZDC) with residual Co nanoparticles was incorporated with TiO_2 composite and adopted as a photocatalyst for the preparation of C_{2+} oxygenates.[48] The ZDC photocatalyst tended to form acetaldehyde, while the ZDC/TiO_2 composite had a good selectivity in production of acetone. The active site and charge dynamics were responsible for the proposed reaction mechanism, in which the C=O intermediates remained on neighboring ZDC sites (Co or pyridinic N) and underwent the reduction steps for producing required multi-carbon oxygenates (Fig. 3e). In this catalytic process, the efficiency was largely restricted by the unfavored multi-electron reaction dynamics. To relieve the kinetically challenging multi-electron reaction conditions in photocatalytic CO_2 reduction, Sun *et al.* reported the synthesis of ultrathin WO_3 $0.33H_2O$ nanotubes with a large amount of surface oxygen vacancy (Vo) sites exposed.[49] The single Vo sites with abundant localized electrons provided enhanced and stable CO_2 photoreduction in pure water under solar light conditions, leading to production of CH_3COOH. The selectivity for CH_3COOH generation was up to 85%, with an average productivity of ~9.4 μmol g^{-1} h^{-1} (Fig. 3f).

Binary metal atomic sites have also been investigated to tune the selectivity. For example, Yu *et al.* reported the incorporation of MoS_2 nanosheets into hierarchically porous defective UiO-66 to form Mo–O–Zr bimetallic sites on the interfaces between UiO-66 and MoS_2.[50] The Mo–O–Zr active interfaces favored the efficient transfer of photo-generated carriers for promoting activity, whereas the synergy of those components at the interfaces enhanced the selectivity for producing CH_3COOH. The evolution rate and selectivity of CH_3COOH reached 39.0 μmol g^{-1} h^{-1} and 94%, respectively, and no C1 products were observed.

The conversion from CO_2 to liquid ethanol is another hotspot in this research area. Wang *et al.* proved that the formation of Cu single atoms on a porous UiO-66-NH_2 support with CO_2 adsorption capabilities allowed to boost the solar-driven conversion of CO_2 to methanol and ethanol with evolution rates of 5.33 and 4.22 μmol g^{-1} h^{-1}, respectively,[51] higher than those of the pristine UiO-66-NH_2 and Cu nanoparticle-decorated UiO-66-NH_2 composites. The increased methanol and ethanol production was ascribed to the cooperation of Cu single atoms with UiO-66-NH_2-derived porous support, which facilitated the conversion of CO_2 to *CHO and *CO intermediates. Recently, the theoretical calculations have predicted a nitrogen-rich C_3N_5 photocatalyst capable of promoting the CO_2 photoconversion to methane and ethanol,[52] but the experimental preparation of this C_3N_5 photocatalyst and the subsequent CO_2 photoreduction experiments are waiting to be demonstrated.

Hydrogenation can also be used to promote the products of ethane, ethylene, acetaldehyde, acetone, acetic acid and ethanol in photocatalytic CO_2 conversion. Under UV-vis excitation, Chen *et al.* reported the CO_2 hydrogenation on CoFe catalysts,[53] and found that the reduction temperature for pre-

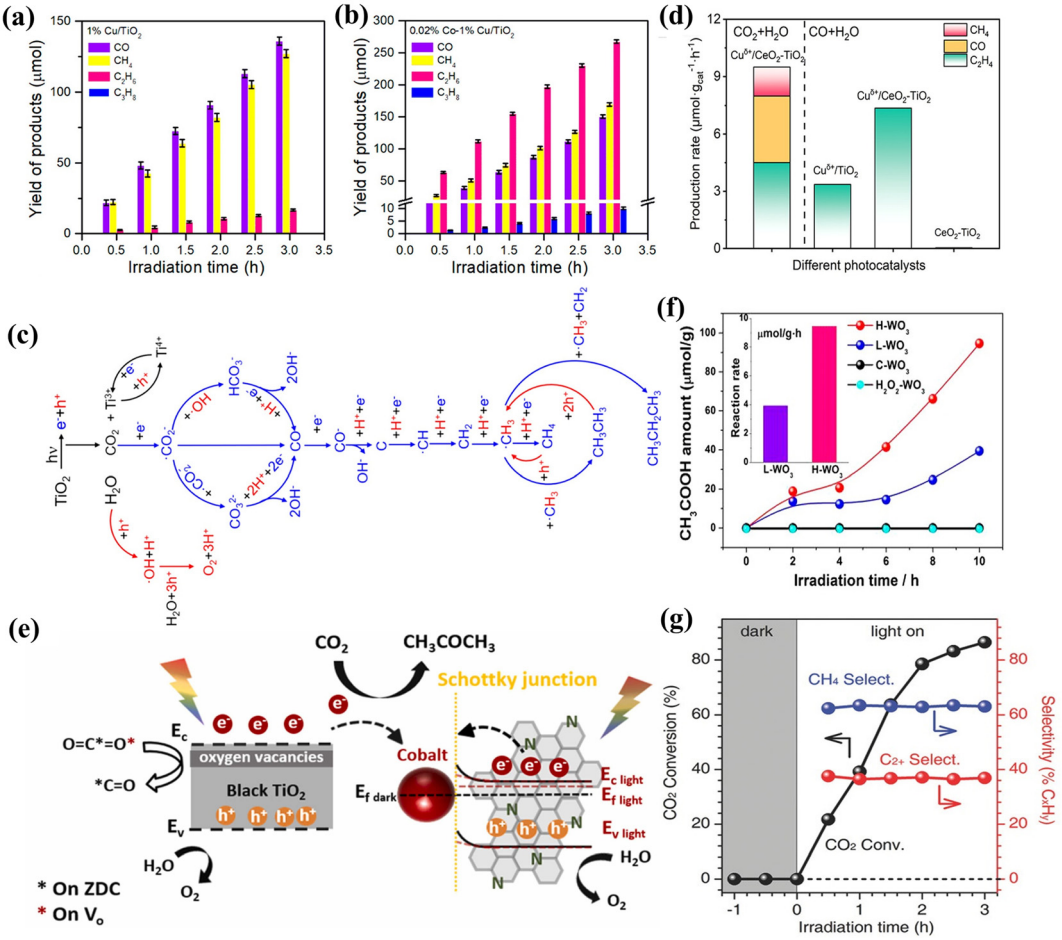

Fig. 3 The distribution of high-valuable multi-carbon oxygenates over (a) 1% Cu/TiO_2 and (b) 0.01% Co–1% Cu/TiO_2 catalyst and (c) possible reaction pathways for photoreduction of CO_2 to methane, ethane and propane, respectively.[46] Copyright 2019, American Chemical Society. (d) Photocatalytic CO_2 reduction to ethylene over $Cu^{\delta+}/CeO_2-TiO_2$.[47] Copyright 2022, American Chemical Society. (e) Schematic illustration of the photocatalytic CO_2 conversion to acetone over ZDC/Ts catalysts.[48] Copyright 2022, Elsevier. (f) Photocatalytic evolution of acetum along with irradiation times in pure water.[49] Copyright 2018, American Chemical Society. (g) Efficiency of photocatalytic CO_2 conversion and selectivity of methane and C_{2+} products over CoFe-650 under UV-vis irradiation.[53] Copyright 2018, Wiley-VCH.

paring the CoFe catalyst influenced the product distributions. With the reduction temperature increased, the CoFe catalyst showed a progressive selectivity shift from CO to CH_4, and eventually to C_{2+} hydrocarbons. The optimal CoFe catalyst showed a combined selectivity of 60% CH_4 and 35% C_{2+} products (Fig. 3g).

In addition, the production of C1 or C_{2+} products can also be affected by experimental conditions, such as incident light. To identify this, Hao *et al.* prepared a $C@Fe_2C/TiO$ ternary composite catalyst by reducing organic compounds under an ammonia atmosphere.[54] The obtained ternary photocatalyst exhibited a high activity under simulated sunlight with the main product of C_2H_4 at a rate of ~35.5 μmol g^{-1} h^{-1} during CO_2 photoreduction. Although the catalytic conversion still proceeded under near-infrared lights irradiation, the main product turned to be CH_4 (18.3 μmol g^{-1} h^{-1}).

To summarize this section, a general strategy for obtaining C_{2+} products in CO_2 photoreduction reactions is the rational fabrication of multiple reaction sites, including bimetallic structures, metal–nonmetal sites, and even cation or anion vacancies. The photocatalytic systems that have been reported to reduce CO_2 into C_{2+} products are listed in Table 2.

3.2.2 Understanding the challenges in obtaining multi-carbon oxygenates. From the number of articles that have been reported for photocatalytic CO_2 reduction to C1 *versus* C_{2+} products, it is clear that the direct conversion of CO_2 into C_{2+} oxygenates is much more challenging, while the reasons have yet to be systematically discussed. Here we analyze and summarize the literatures by covering three fundamental features of the multi-electron-coupled-proton-transfer process, the electron storage and charge separation, and the diversity of pathway selection of intermediates in photocatalytic CO_2 reduction reactions.

First, the CO_2 photoreduction and product selectivity strongly depend on the lifespan of photoexcited charge carriers. Generally, the production of C_{2+} oxygenates needs more

Table 2 Summary of photocatalytic conversion of CO_2 into multi-carbon products

Photocatalyst	Major products	Reaction conditions	Ref.
Pd–TiO_2	6.4% C_2H_6	300 W Xe lamp, 5 h	55
Au–Pd/TiO_2	7% C_2H_6 + 7% C_2H_4	300 W Xe lamp	56
Pt–graphene/TiO_2	22.9% C_2H_6	100 mW cm^{-2}, flow reactor	57
Au/TiO_2	27% C_2H_6	Hg lamp, 254 nm, 20 mW cm^{-2}	58
CdS/Cu-trititanate nanotubes	31.1% C_2H_6	450 W Xe lamp, 5 h	59
CoFe-Based catalysts	35% C_{2+}	300 W Xe lamp, 2 h	53
Au NPs	40% C_2H_6	λ > 488 nm, 750 mW cm^{-2}	60
0.02% Co–1% Cu/TiO_2	45.6% C_2H_6	300 W Xe lamp, 3 h	46
Au/ZnO	80% C_2H_6	300 W Xe lamp, 6 h	61
Carbon/TiO_2	51.8% CH_3COCH_3	150 W solar simulator, 6 h	48
Carbon nanotube/TiO_2	69.7% CH_3CH_2OH	UV lamp, 365 nm, 5 h	62
$Cu^{\delta+}$/CeO_2–TiO_2	73.9% C_2H_4	Xe lamp, 200 mW cm^{-2}, 5 h	47
Rh-Doped TiO_2	78.4% CH_3CHO	Xe lamp, 362 mW cm^{-2}, 6 h	63
WO_3 0.33H_2O	85% CH_3COOH	100 mW cm^{-2}, 10 h	49
Pt/TaON	89.5% CH_3CH_2OH	λ > 420 nm, 1002 W m^{-2}	64
15 wt% Cu/GO	100% CH_3CHO	Halogen lamp, 100 mW cm^{-2}	65
Cu_2O/graphene	100% CH_3CH_2OH	Hg lamp, 254 nm, flow reactor	66
C@Fe_2C/TiO	87.5% C_2H_4	300 W Xe lamp, 4 h	54
Polymeric C_3N_4	98.3% CH_3CHO	5 W LED lamp, 4 h	67
d-UiO-66/MoS_2	94% CH_3COOH	300 W Xe lamp, 100 mW cm^{-2}	50
Cu SAs/UiO-66-NH_2	44% CH_3CH_2OH	300 W Xe lamp	51
Ni-Nanocluster loaded black TiO_2	~100% CH_3CHO	300 W halogen lamp	68

electrons and protons during reactions, and the multi-electron-coupled-proton-transfer process and subsequent C–C coupling are considered as critical elementary steps.[69] The electron–hole recombination can significantly reduce this process, resulting in a decreased conversion reactivity of CO_2 and modified selectivities toward C1 products with fewer required electrons. When the lifespan of electrons is long enough by inhibiting the recombination between electrons and holes, the possibility of electrons for reducing CO_2 molecules into C_{2+} oxygenates is enhanced. The migration of active electrons regularly happens in a short period time. The kinetics of charge separation in time scale and utilization of electrons and protons to form different products are summarized (Fig. 4a).[70] The typical time scale for charge transfer in photocatalytic CO_2 reduction to different products ranges from nanoseconds to microseconds, which requires longer time when more electrons and protons are needed in generating the products. The numbers of required electrons and protons and the corresponding standard redox potentials in photocatalytic CO_2 reduction to different products are listed in Table 3. The reactions leading to C_{2+} oxygenates require >8 electrons and protons. However, in contrast to electrocatalysis with continuous and stable electron supply, photocatalysis is substantially affected by the short electron lifetime and limited numbers of electrons. Thus, in order to promote the selectivity of multi-carbon oxygenates, the reaction conditions and materials designs should favor the generation and storage of photo-induced electrons.

Apart from the importance of accumulating abundant electrons required in multi-electron-coupled-proton-transfer process, the charge separation efficiency is significant for generating C_{2+} products.[74] In a semiconductor, charge carrier migration normally occurs *via* random pathways, which can lead to the high probability of the carrier recombination. To

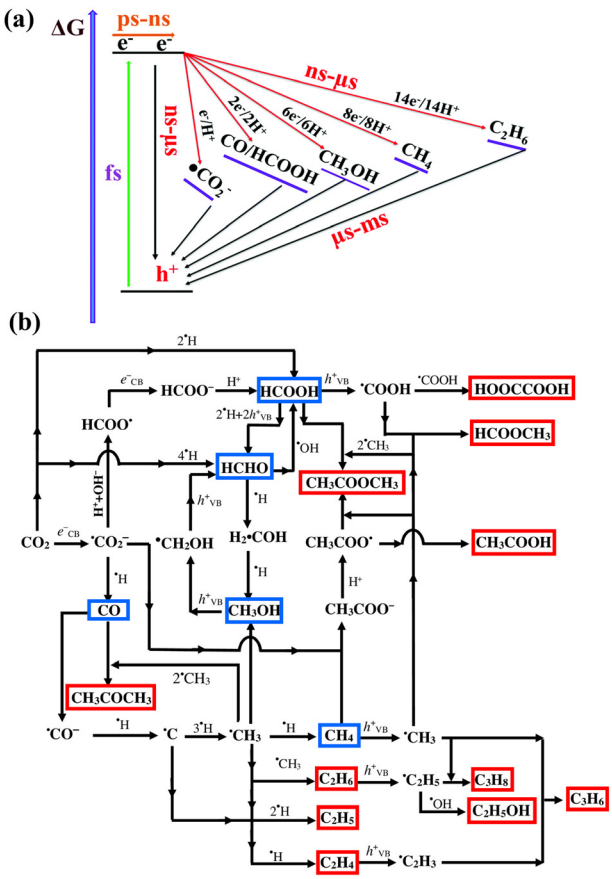

Fig. 4 (a) The required timescale and range of the charge transfer in photocatalytic CO_2 reduction to produce C1 and multi-carbon oxygenates.[70] Copyright 2022, Royal Society of Chemistry. (b) The proposed pathways of photocatalytic CO_2 into C1 (blue wireframes) and multi-carbon products (red wireframes).[77] Copyright 2016, Elsevier.

Table 3 Standard redox potentials and required electrons and protons to form C1 products and multi-carbon oxygenates in photocatalytic CO_2 reduction reaction[71–73]

Reactions	E° (V *vs.* NHE)	Products
$CO_2 + e^- \rightarrow CO_2^{\bullet-}$	−1.90	—
$CO_2 + 2H^+ + 2e^- \rightarrow CO + H_2O$	−0.51	CO
$CO_2 + 2H^+ + 2e^- \rightarrow HCOOH$	−0.58	HCOOH
$CO_2 + 4H^+ + 4e^- \rightarrow HCHO + H_2O$	−0.55	HCHO
$CO_2 + 6H^+ + 6e^- \rightarrow CH_3OH + H_2O$	−0.39	CH_3OH
$CO_2 + 8H^+ + 8e^- \rightarrow CH_4 + 4H_2O$	−0.24	CH_4
$2CO_2 + 8H^+ + 8e^- \rightarrow CH_3COOH + H_2O$	−0.31	CH_3COOH
$2CO_2 + 10H^+ + 10e^- \rightarrow CH_3CHO + 3H_2O$	−0.36	CH_3CHO
$2CO_2 + 12H^+ + 12e^- \rightarrow C_2H_5OH + 3H_2O$	−0.33	C_2H_5OH
$2CO_2 + 12H^+ + 12e^- \rightarrow C_2H_4 + 4H_2O$	−0.34	C_2H_4
$2CO_2 + 14H^+ + 14e^- \rightarrow C_2H_6 + 4H_2O$	−0.27	C_2H_6
$3CO_2 + 16H^+ + 16e^- \rightarrow CH_3CH_2CHO + 5H_2O$	−0.32	CH_3CH_2CHO
$3CO_2 + 16H^+ + 16e^- \rightarrow CH_3COCH_3 + 5H_2O$	−0.31	CH_3COCH_3

suppress the recombination rate of electron–hole pairs by driving forces, many strategies, including the design of atomic-scale structures, defect states, surface polarization and built-in electric fields in photocatalysts have been developed.[75] The attention of noble metal in boosting charge separation is another key point, as the noble metals have superior abilities to carry electrons.[76] Overall, the establishment of large driving forces to separate electrons and holes is critical.

The diversity of pathway selection of intermediates in photocatalytic CO_2 reduction reactions is another critical factor. As shown in Fig. 4b, the establishment of $^\bullet CO_2^-$ is typically the first step to trigger photocatalytic CO_2 reduction reactions.[77] The $^\bullet CO_2^-$ intermediate either undergoes a protonation or disproportionation to selectively produce C1 products, or dimerize into the C_{2+} products. The secondary reaction intermediates originated from $^\bullet CO_2^-$ include $^\bullet CO^-$, $HCOO^-$ and $^\bullet CH_3$, which either produce corresponding C1 products after coupling with protons and electrons, or transform into subsequent intermediates such as CH_3COO^- and $^\bullet C_2H_5$, which can further undergo C–C coupling steps. From this point of view, C1 products are relatively easy to obtain, while the C_{2+} oxygenates require multi-step transformation of intermediates and complex pathways. To date, most of the efforts for promoting C–C coupling among tertiary intermediates have been focusing on designing active sites of photocatalysts, which will be discussed in Section 4.3.

3.2.3 CO_2 reacts with other molecules to form multi-carbon oxygenates. In addition to converting individual CO_2 molecules, the interest in studying CO_2 with other molecules to promote the production of C_{2+} oxygenates has also arisen recently, especially in the aspects of organic synthesis through designing synergistic redox reaction systems.[78] In this section, we will discuss those photocatalytic systems based on heterogeneous photocatalysis and the coupling of CO_2 conversion with organic synthesis.

At present, this research area mainly includes two major strategies.[79] One is the integration of photocatalytic CO_2 utilization with organic synthesis, for increasing utilization of electron–hole pairs. For example, Guo *et al.* reported the CO_2 reduction integrated with oxidative organic synthesis using solar energy (Fig. 5a).[80] At the presence of triethylamine, the synthesized CdSe/CdS quantum dots enabled photocatalytic conversion of CO_2 to CO with a high selectivity (>96%) and a yield of pinacol production (>98%) under visible-light irradiation (Fig. 5b). Another strategy in achieving the insertion of CO_2 is the photocatalytic activation of organic molecules or intermediates.[81] If organic molecules are converted by photogenerated holes into active organic intermediates, this may enable higher efficiencies of reacting with CO_2 or CO_2 intermediates (*i.e.*, *CO) to form C–C or C–N bonds. Han *et al.* disclosed that the benzylamine, in addition to the traditional deprotonation process, could react with CO_2 to produce benzylcarbamic acid intermediate as an efficient electron donor to complete the redox cycle,[82] suggesting an upgraded cooperation between CO_2 reduction and amine oxidation that facilitated the bidirectional reaction toward C–N coupling (Fig. 5c). The CO_2 intermediate has also been reported in synthesizing different valuable C_{2+} oxygenates. As shown in Fig. 5d, the generated $^\bullet CO_2^-$ intermediates were capable of reacting with the acetylacetone radicals that were originated from the acetylacetone oxidation by photoinduced holes.[83] Then $^\bullet CO_2^-$ and acetylacetone radicals were coupled to form the target carboxylic acids. Thus, the reaction of CO_2 with other substrates is a potential direction in driving the synthesis of multi-carbon oxygenates under light irradiation by utilizing CO_2 as a carbon source.

In this section, we summarize the progress of photocatalytic CO_2 conversion into multi-carbon products, where the design concepts of multiple reactive sites to deliver more electrons are frequently-used. However, the slow multi-electron-coupled-proton-transfer process, the limited electron storage and charge separation, and the diversity of pathway selection of intermediates in the reactions are still challenging in realizing high conversion efficiency of C_{2+} products from individual CO_2 molecules, requiring further development of more advanced photocatalysts or photocatalytic systems. In addition, the designing of synergistic redox reactions, such as coupling with oxidative organic synthesis and insertion of CO_2 intermediates into organic molecules, represent another potential scenario to facilitate the utilization of electron–hole pairs for the transformation of CO_2 into valuable multi-carbon products.

4. Regulating reaction pathways toward multi-carbon oxygenates

In order to guide the efficient conversion into value-added products, whether it is the direct CO_2 reduction or the reaction of CO_2 with other organic molecules, the whole photocatalytic reduction process is essentially affected by the following four key aspects.

4.1 Photocatalyst design

As stated above, the designed photocatalyst must solve the kinetic threshold of the multi-electron reduction process to

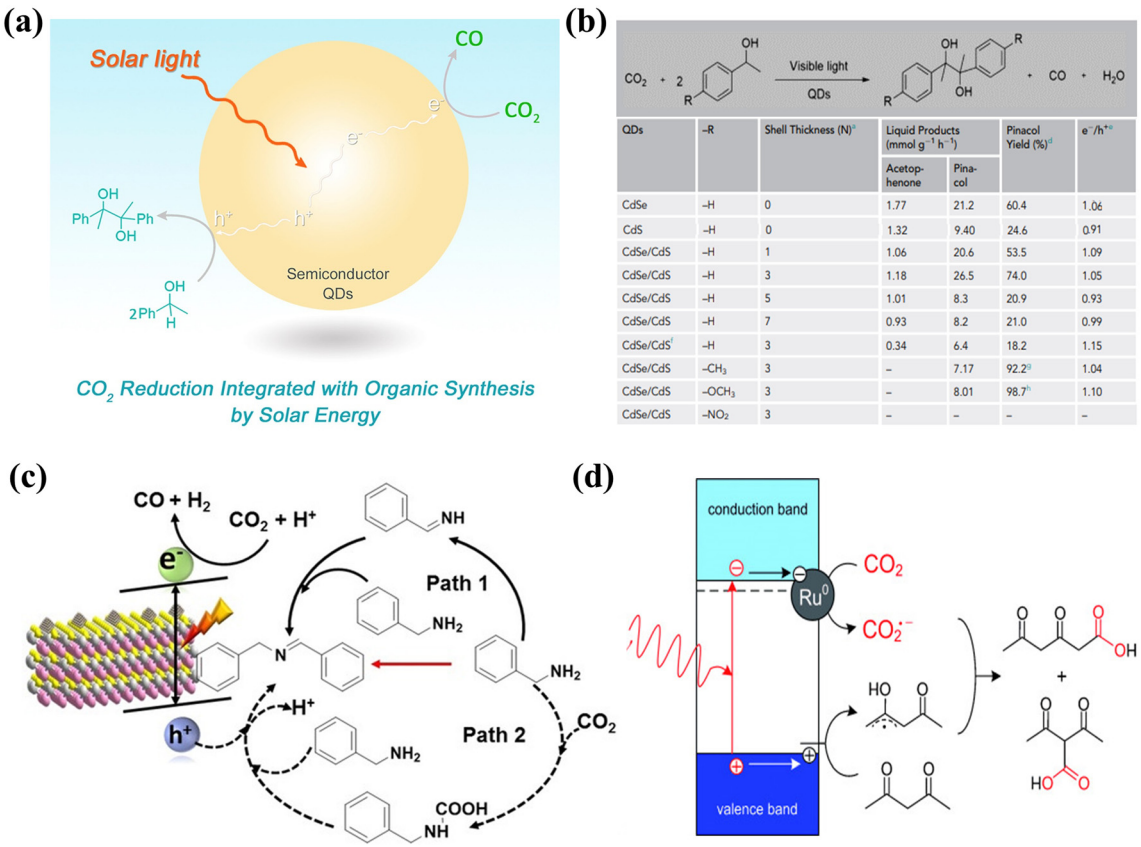

QDs	–R	Shell Thickness (N)[a]	Liquid Products (mmol g^{-1} h^{-1})		Pinacol Yield (%)[d]	e^-/h^+[e]
			Acetophenone	Pinacol		
CdSe	–H	0	1.77	21.2	60.4	1.06
CdS	–H	0	1.32	9.40	24.6	0.91
CdSe/CdS	–H	1	1.06	20.6	53.5	1.09
CdSe/CdS	–H	3	1.18	26.5	74.0	1.05
CdSe/CdS	–H	5	1.01	8.3	20.9	0.93
CdSe/CdS	–H	7	0.93	8.2	21.0	0.99
CdSe/CdS[f]	–H	3	0.34	6.4	18.2	1.15
CdSe/CdS	$-CH_3$	3	–	7.17	92.2[g]	1.04
CdSe/CdS	$-OCH_3$	3	–	8.01	98.7[h]	1.10
CdSe/CdS	$-NO_2$	3	–	–	–	–

Fig. 5 (a) Photocatalytic CO_2 reduction coupled with oxidative organic synthesis by semiconductor quantum dots and (b) visible-light-driven CO_2 reduction integrated with pinacol coupling reaction.[80] Copyright 2019, Elsevier. (c) Schematic of photocatalytic CO_2 reduction paired with selective benzylamine oxidation for the production of C–N coupling products.[82] Copyright 2021, Wiley-VCH. (d) A possible mechanism for the photocatalytic carboxylation of acetylacetone with CO_2.[83] Copyright 2014, Wiley-VCH.

favor the conversion of CO_2 into multi-carbon oxygenates. Thus, the discovery of photocatalysts with efficient photoadsorption and charge separation capability should be rationally investigated, including bandgap engineering, nanostructure design, heterostructure fabrication, defect engineering, and cocatalyst loading. For example, Chen *et al.* tailored the bandgap structures of graphene quantum dots, making them suitable for water splitting and CO_2 reduction under visible light (Fig. 6a).[84] Wang *et al.* constructed highly dispersed nickel cobalt oxyphosphide nanoparticles that were confined in multi-channel hollow carbon fibers,[85] which provided a high conductivity for promoting the mass/charge transfer efficiency (Fig. 6b). The schematic illustration of the conversion of CO_2 into products was shown in Fig. 6c. On the other hand, many studies also focus on the heterostructure designs.[86–88] For example, a ZnSe nanorods–$CsSnCl_3$ perovskite (ZnSe–$CsSnCl_3$) type-II heterojunction was fabricated,[89] which exhibited efficient charge separation and a lowered free energy for CO_2 reduction (Fig. 6d). A Z-scheme system was constructed by using a graphite phase carbon nitride (g-C_3N_4) shell encapsulating Cu_2O nanowire arrays/Cu mesh to boost the charger separation efficiency in photocatalytic CO_2 conversion (Fig. 6e).[90]

The defect engineering is another useful way for fast charge separation efficiency in photocatalytic CO_2 conversion. For instance, $Bi_{12}O_{17}Cl_2$ superfine nanotubes with bilayer tube walls were fabricated to achieve structural distortion for creating surface oxygen defects, which accelerated carrier migration and facilitated CO_2 activation (Fig. 6f).[91] In addition, co-catalysts were generally deposited in the form of nanoparticles on the catalyst surface.[92,93] For example, an isolated single-atom Rh acting as dopants in two-dimensional titanium oxide crystals was prepared as the co-catalyst for the efficient separation of chargers (Fig. 6g).[94] Recently, Long and coworkers reported Au nanoparticle-loaded TiO_2 photocatalysts for the extraction of photogenerated electrons toward CO_2 photoreduction.[95] The aforementioned studies suggest strategies for enhancing the charger separation efficiencies, thus capable of providing more electrons to convert CO_2 into multi-carbon oxygenates.

4.2 Mass transfer control

The mass transfer in the photocatalytic systems should also be efficiently elevated for accelerating the migration of electrons and protons toward the production of C_{2+} oxygenates. For example, a gas flow-through photocatalytic reactor was developed using copper-functionalized nanomembranes for the

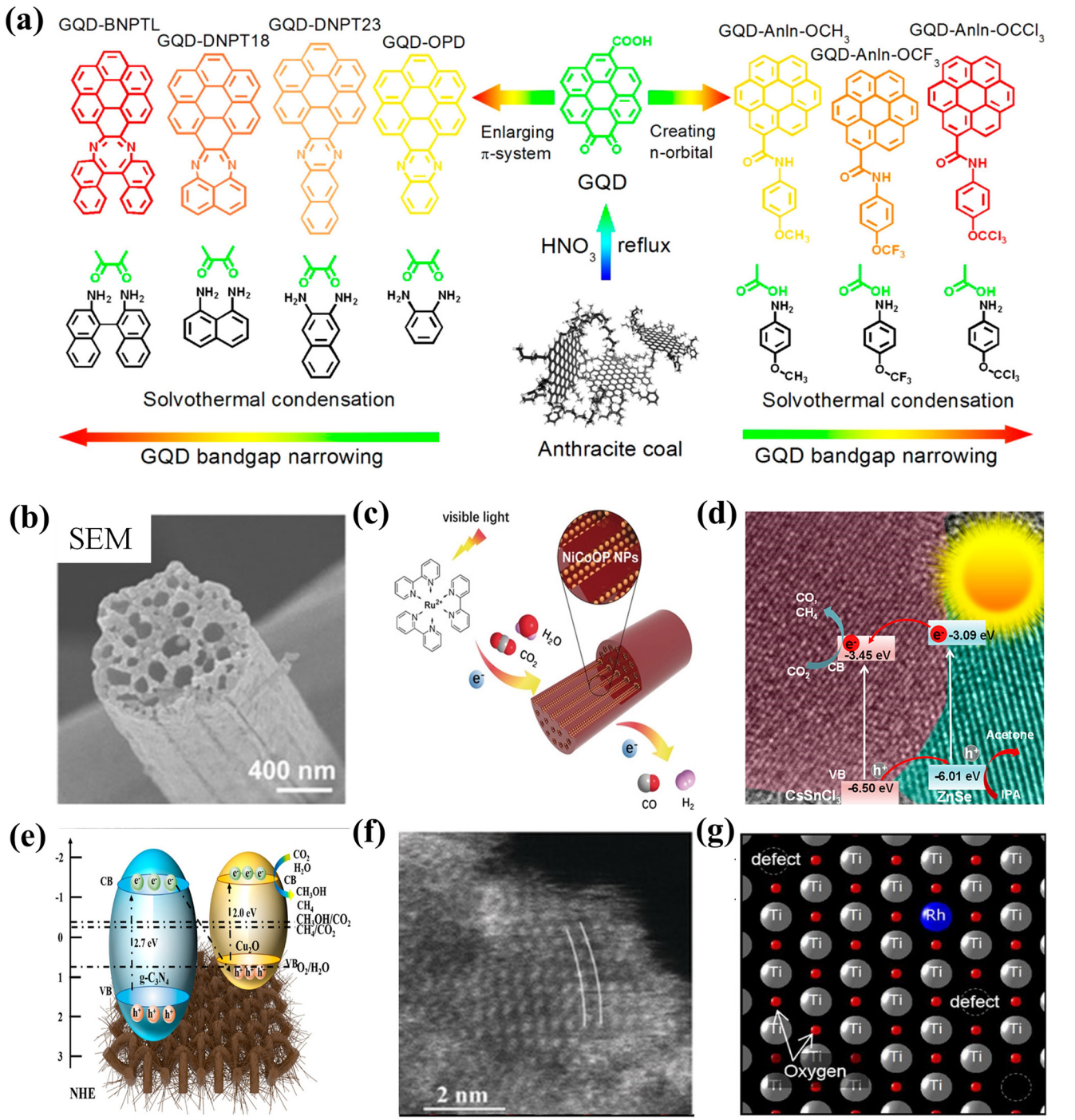

Fig. 6 (a) Illustration of bandgap narrowing by enlarging π-conjugated system *via* conjugating graphene quantum dots with poly aromatic rings (left panel) or by introducing intermediate n-orbital *via* conjugating with electron-donating groups (right panel).[84] Copyright 2018, American Chemical Society. (b) Scanning electron microscopy (SEM) images of synthesized nickel cobalt oxyphosphide nanostructures and (c) schematic illustration of the conversion of CO_2 into products.[85] Copyright 2019, Wiley-VCH. (d) Photocatalytic mechanism of the ZnSe–$CsSnCl_3$ heterojunction composite for CO_2 reduction.[89] Copyright 2022, American Chemical Society. (e) Schematic diagram of the 3D spatial reticulation all-solid-state direct Z-scheme heterostructure.[90] Copyright 2020, American Chemical Society. (f) Aberration-corrected high-angle annular dark field with scanning transmission electron microscopy (HAADF-STEM) images of $Bi_{12}O_{17}Cl_2$ nanotubes.[91] Copyright 2018, Wiley-VCH. (g) The atomic structural model consists of 1 Rh atom, 28 Ti atoms, and 3 vacancy-like defects.[94] Copyright 2015, American Chemical Society.

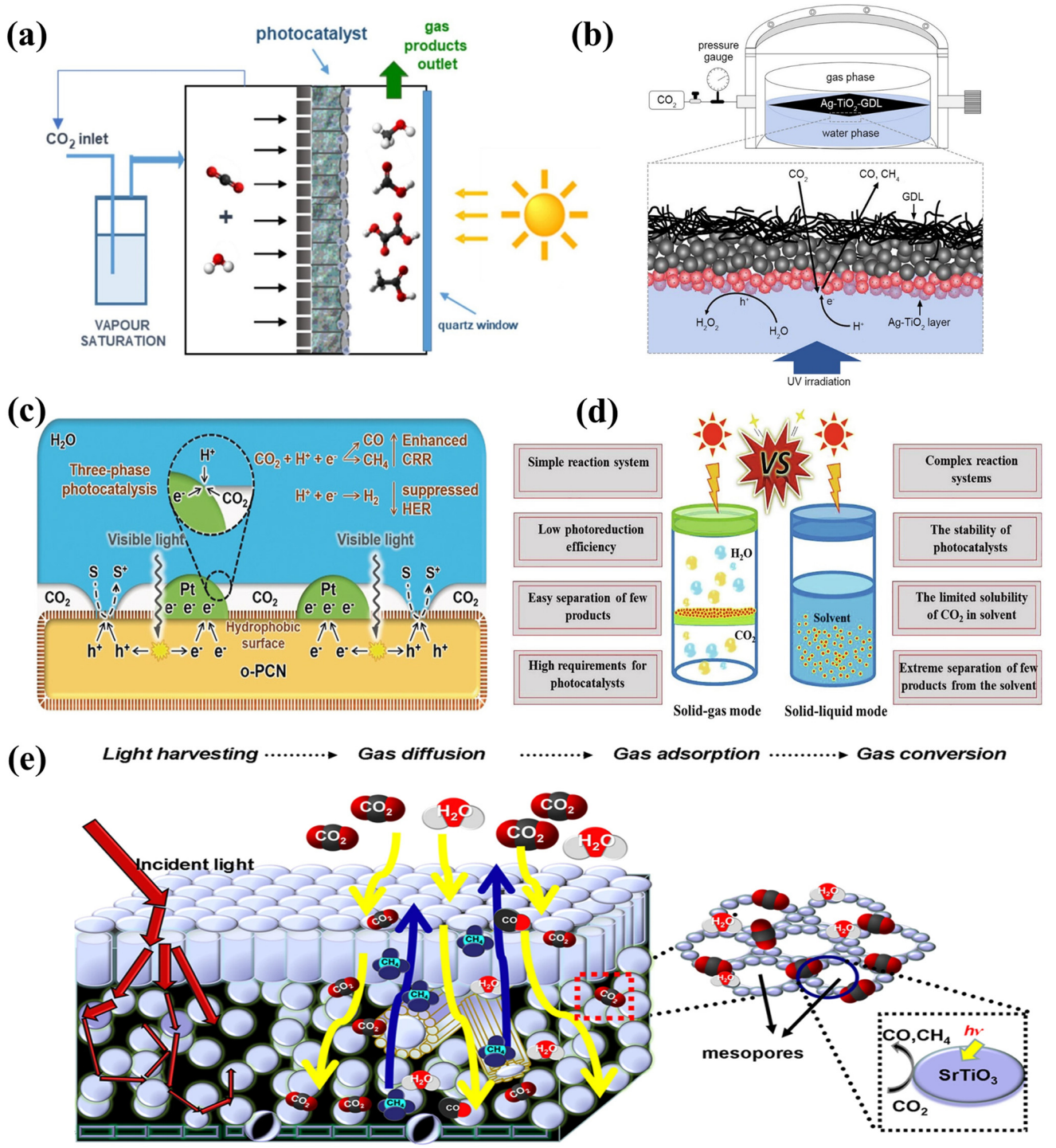

Fig. 7 (a) Illustration of a flow-through reactor for photocatalytic CO_2 reduction.[96] Copyright 2021, Elsevier. (b) Schematic illustration of the photocatalytic CO_2 reduction system based on Ag–TiO_2 supported at the gas–water boundary.[97] Copyright 2022, Wiley-VCH. (c) The mechanism of three-phase photocatalysis for boosting mass transfer.[98] Copyright 2019, Wiley-VCH. (d) The comparison of advantages and disadvantages between solid–gas mode and solid–liquid mode.[71] Copyright 2021, Elsevier. (e) Schematic diagram of artificial photosynthetic system to accelerate reactant flow. The process includes light harvesting, gas diffusion/adsorption, and gas conversion.[99] Copyright 2013, Springer Nature.

conversion of CO_2 to C_{2+} oxygenates (Fig. 7a).[96] The nanomembranes consisted of aligned TiO_2 nanotube arrays grown on a metallic substrate, which acted as an electron collector for providing necessary robustness. Unlike the traditional solid–liquid reaction model, the designed photoreactor functioned under a cross-flow of gaseous CO_2 pre-saturated with water that were delivered through the nanomembrane photocatalyst layer, which was able to achieve selective CO_2 conversion to

formic, acetic and oxalic acids. This design concept of nanomembranes in a gas flow-through system is similar to the utilization of membrane-derived vesicles in producing C1 products (CH_4 and CO),[32] but more efficient with a high selectivity to formic acid and acetic acid. In a similar way, Huang *et al.* developed a three-phase photocatalytic CO_2 reduction system with Ag-modified TiO_2 nanoparticles at the gas–water interface (Fig. 7b).[97] The gas–liquid–solid three-phase interface promoted the transfer of gas-phase CO_2 to the surface of photocatalyst, while maintaining high-efficiency water supply and uncovered active sites. Even without hole scavengers, the CO_2 photoreduction rate was approximately 8 times higher than the nanoparticles dispersed in the liquid phase, providing a strategy for boosting the interfacial CO_2 mass transfer. Similarly, a photocatalyst with hydrophobic surfaces was reported, in which the fabrication of hydrophobic surfaces facilitated efficient three-phase contact of CO_2, H_2O and catalyst.[98] The concentrated CO_2 molecules in the gas phase can contact the catalyst surface directly and overcome the mass-transfer limitation of CO_2, leading a powerful inhibition of hydrogen evolution reactions (HER) and enhancing CO_2 reductions (Fig. 7c). Even loaded with Pt nanoparticles, the three-phase photocatalyst retained adequate contact of CO_2 and maintained a CO_2 selectivity of 87.9%.

The comparisons of CO_2 photoreduction both in the solid–liquid or solid–gas modes are summarized in Fig. 7d. It can be seen that most of the previous reports have adopted the solid–liquid mode for CO_2 photoreduction, while the limitation of CO_2 solubility in water restricts the mass transfer severely and hinders photocatalytic efficiency.[71] In contrast, the introduction of solid–gas mode allows to avoid this drawback and thus promotes the performance of CO_2 photoreduction. Zhou *et al.* designed an artificial photosynthetic system for enhancing mass flow (*e.g.*, CO_2, O_2, and H_2O) and light harvesting, in which perovskite titanates ($ATiO_3$, A = Sr, Ca, and Pb) were applied to mimic the structure of leaves (Fig. 7e).[99] In addition to the accelerated gas flow for mass transfer, the artificial structure also provided efficient diffusion and adsorption of the reactants and desorption of the products. This nature-inspired structure can be attractive in solving slow mass transfer efficiency in photocatalytic CO_2 reduction for producing multi-carbon oxygenates.

4.3 Determination of active sites

In comparison to the C1 products, the formation of multi-carbon oxygenates is more challenging, as their production strongly depends on the participation of multiple active sites in addition to the dynamics of chargers and diversity of reaction pathways.[100] The active sites are commonly composed of monodispersed metals, which are responsible for stabilizing different intermediates of CO_2 and facilitating C–C coupling in photoreduction reactions. The basic C–C coupling process induced by active sites are presented in Fig. 8, where the key point lies in the influences of monodispersed metals on the adsorption and coupling of CO_2 or carbon intermediates on the surface of catalysts. First, the compositions of active sites affect the adsorption of intermediates. For example, Li *et al.* illustrated that the Au sites in AuCu alloys benefited the adsorption of CO_2 molecules, while the promoted formation of *CO intermediates was observed on the Cu sites.[101] The subsequent C–C coupling step was completed by *CO dimerization to yield CH_3CH_2OH. In a Nb_2O_5/g-C_3N_4 catalyst, the introduction of Nb-sites allowed to increase the adsorption of other intermediates, such as *CHO.[102] In a WO_3/$BiVO_4$ catalyst, the Bi-sites was favorable for the absorption of *CH_2O intermediates.[103] Second, the distance between active sites can tune the C–C coupling reactions. Zhao and colleagues proposed that the close distance of dual Cu atomic sites promoted the electron density redistribution, and is thus active for triggering C–C coupling.[104]

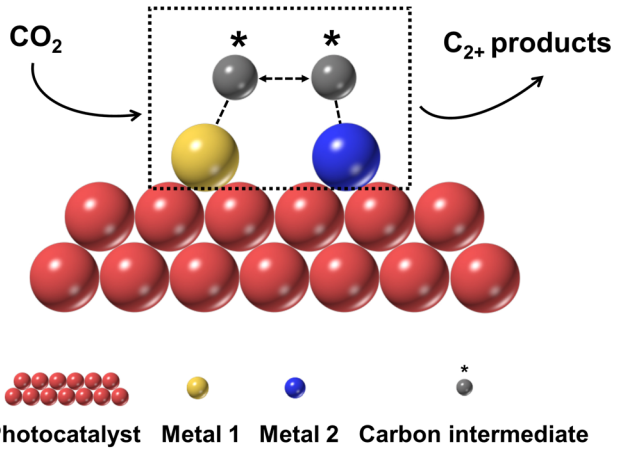

Fig. 8 The C–C coupling process induced by active sites.

Considering the importance of active sites in C–C coupling reactions, the determination of active sites in photocatalysts should be critically studied. For the design of active sites, Billo *et al.* reported the Ni-nanocluster loaded black TiO_2 with dual active sites enabled selective photocatalytic CO_2 conversion to C_{2+} oxygenates.[68] The accessible oxygen vacancies within TiO_2 and metallic Ni served as favorable active sites for CO_2 adsorption during photocatalytic reduction, leading to high activity (10 μmol g^{-1} h^{-1}) and selectivity (~100%) for acetaldehyde production (Fig. 9a and b). To create vacancy-coupled metal sites, the aforementioned defect engineering and cocatalyst loading are also effective methods.[105,106] For the determination of active sites, Hu *et al.* identified the dynamic coordination and electronic structures of a Ni complex catalyst in a homogeneous photocatalytic system for CO_2 reduction by time-resolved X-ray absorption spectroscopy (TR-XAS).[107] The reduced Ni(I) intermediate was coordinated with a terpyridine ligand, CO_2, and CH_3CN solvent to generate a five-coordinated Ni(tpy)(CO_2)(CH_3CN) species, which served as the active species in photocatalytic CO_2 conversion (Fig. 9c and d). In another work, Wang *et al.* revealed the structure of Cu–Ce dual active sites ($Cu^{\delta+}$/CeO_2–TiO_2) using X-ray absorption fine structure (XAFS) technology (Fig. 9e and f).[47] The function of TiO_2 in this system was considered as a light-harvesting material for

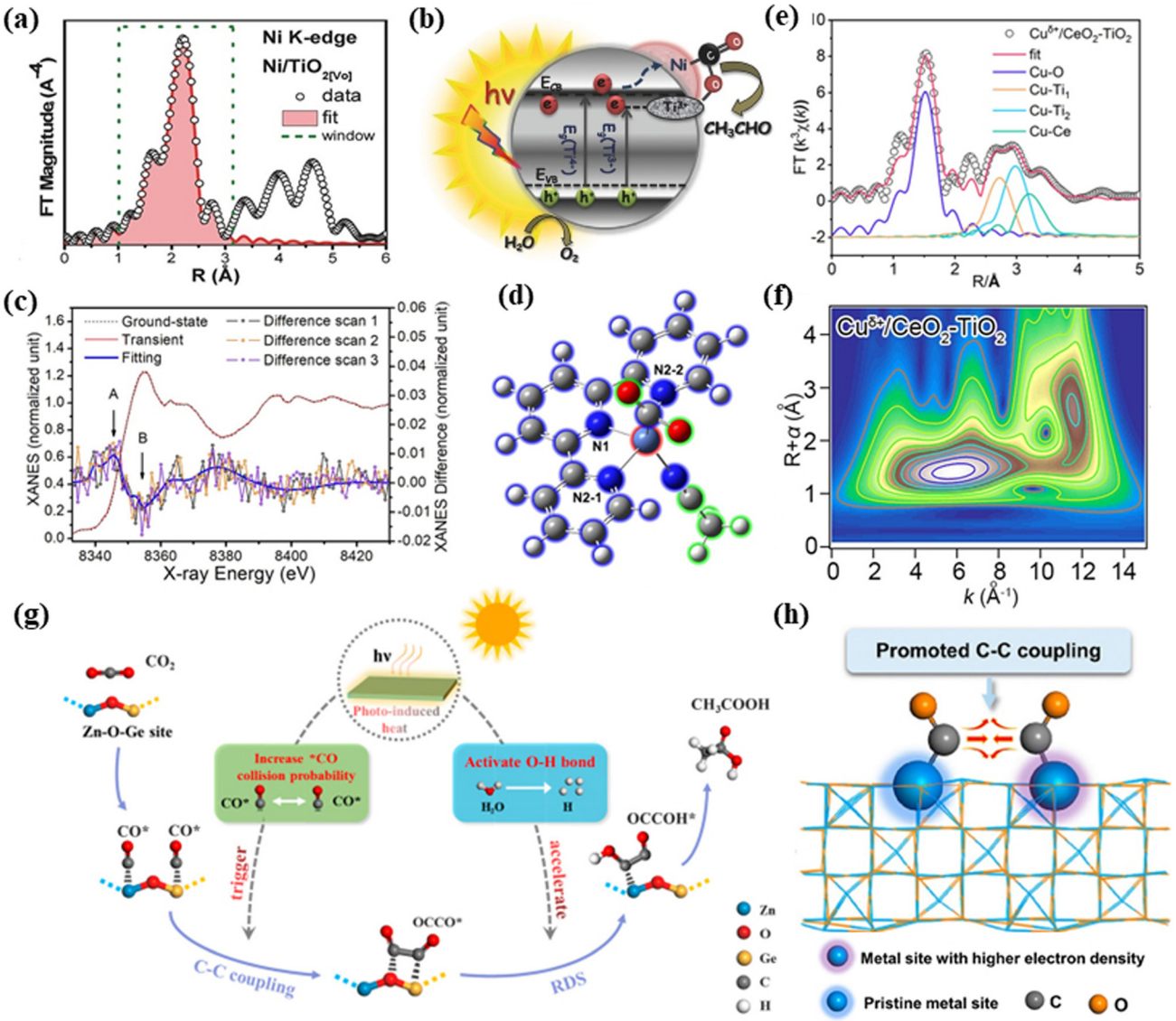

Fig. 9 (a) Fourier-transform extended X-ray absorption fine structure (FT-EXAFS) spectra of k^3-weighted Ni K-edge and (b) illustration of photocatalytic CO_2 reduction by Ni-nanocluster loaded black TiO_2 as dual active sites.[68] Copyright 2017, Wiley-VCH. (c) Transient X-ray absorption near-edge structure (XANES) spectrum (red) at 0.4 μs after laser excitation and ground-state spectrum (black dotted line) and (d) the optimized structure of Ni intermediate.[107] Copyright 2020, American Chemical Society. (e) FT-EXAFS spectra and (f) wavelet-transform (WT)-EXAFS for the k^3-weighted Cu K-edge.[47] Copyright 2022, American Chemical Society. (g) The schematic illustration of Zn–O–Ge sites for boosting CO_2 reduction to CH_3COOH.[108] Copyright 2021, American Chemical Society. (h) The designed charge-polarized metal pair sites for promoting C–C coupling to yield multi-carbon oxygenates.[109] Copyright 2021, American Chemical Society.

generating electron–hole pairs, which were then efficiently separated by the formed interfaces between CeO_2 and TiO_2. The Cu–Ce dual active sites in CeO_2/TiO_2 interface synergistically facilitated the generation and dimerization of *CO intermediates, benefiting the lower energy barrier of C–C coupling. Zhu *et al.* reported the asymmetric Zn–O–Ge tri-atomic sites that were confined inside phenakite to facilitate the C–C coupling by alleviating electrostatic repulsion, and then employed photoinduced heat to increase molecular thermal vibration, resulting in accelerated CO_2 reduction to acetic acid with a stability of up to 220 hours.[108] The schematic illustration of Zn–O–Ge sites for accelerating different charge distributions in adjacent *CO intermediates and boosting CO_2 reduction to CH_3COOH was shown in Fig. 9g. Adopting similar strategies, the concept of charge-polarized metal pair sites for triggering C–C coupling through manipulating asymmetric charge distribution was further reported by the same group.[109] Using the partially reduced Co_3O_4 nanosheets, they found that the formed charge-polarized cobalt pair sites not only donated electrons to CO_2 molecules, but also accelerated the coupling of asymmetric *COOH (Fig. 9h). The electron-rich cobalt sites strengthened the interaction with O atoms in the HOOC–

*CH_2O intermediate, which favored the C–O cleavage and facilitated the formation of CH_3COOH.

Furthermore, the presence of metal nanoparticles in photocatalysts may offer additional advantages. Yu *et al.* reported the plasmonic Au nanoparticles benefited the conversion of CO_2 into C1 or C_{2+} products, and the product selectivity was dependent on the mode of plasmonic excitation.[60] The localized surface plasmon resonance (LSPR) bands at 514.5 and 532 nm resulted in a faster charge recombination, and the hot electrons were not capable of coupling reaction. At higher photon energy plasmonic excitations (457.9 and 488 nm), a lower recombination rate of the photoexcited charge carriers was achieved, and the hot electrons in this occasion underwent the C–C coupling to produce C_{2+} products. Generally, the transition metals like Cu, Ni can promote the hydrogenation process and are suitable for the formation of C1 products, whereas the noble metals like Au, Pd, and Ag can contribute to the C–C coupling reactions and favor the production of C_{2+} products.[70] The size, optical properties, and light excitation can also affect the selectivity of C1 products and C_{2+} products.

4.4 Reaction intermediate regulation

By detecting the possible intermediates during the photocatalytic CO_2 conversion process, *in situ* spectroscopic measurements such as Fourier-transform infrared (FT-IR) and Raman spectroscopy are effective approaches to investigate the reaction mechanism. To precisely regulate the reaction toward C_{2+} oxygenates, it is beneficial to obtain the information about dynamic evolution process of possible intermediates, as well as to understand their functions in favoring the formation of targeted products. For instance, Shao *et al.* reported that the Ni^{2+}–$Ni^{\delta+}$ pair sites in prepared Co-doped NiS_2 atomic layers endowed the adjacent CO intermediates with distinctive charge densities, thus decreasing their dipole–dipole repulsion and lowering the rate-limiting C–C coupling reaction barrier.[110] To investigate the influence of Ni^{2+}–$Ni^{\delta+}$ pair sites on the C–C coupling at the molecular level, *in situ* FTIR spectroscopic measurements were utilized to probe the possible intermediates in photocatalytic CO_2 reactions, and the observed intermediates were summarized in Fig. 10a. The emerging peaks at 1219 and 1310 cm^{-1} were attributed to the δ(OH) bending vibration of HCO_3* and the asymmetric OCO

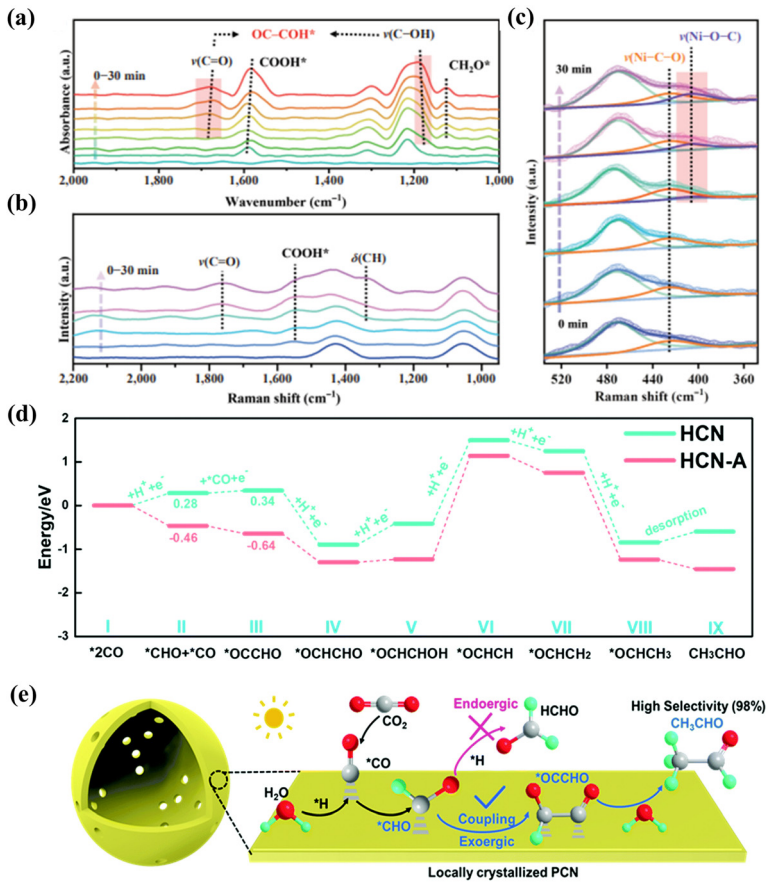

Fig. 10 (a) *In situ* FTIR spectra measurements and (b and c) quasi *in situ* Raman spectra in different Raman shift regions.[110] Copyright 2022, Springer Nature. (d) Calculated free energy diagram for the reduction of CO_2 to CH_3CHO on the hydrothermal-pretreated carbon nitride (HCN) and HCN-A (carbon nitride modified with amino-2-propanol) and (e) proposed reaction mechanism for the photocatalytic CO_2 reduction conversion to CH_3CHO. The grey, red, and green color spheres denote carbon, oxygen, and hydrogen atoms, respectively.[67] Copyright 2022, Royal Society of Chemistry.

stretching of HCO_3*, respectively. The peak at ~1589 cm^{-1} was assigned to the *COOH group, which was a common intermediate during photocatalytic CO_2 reduction to CO, and the intensity gradually increased with the extension of irradiation time. The quasi *in situ* Raman results affirmed the existence of C═O stretching and *COOH groups (Fig. 10b), consistent with the *in situ* FTIR spectra. The peak at 421 cm^{-1} was attributed to the vibrations of Ni–C–O bonds, and the gradually emerging peak at 404 cm^{-1} was ascribed to the vibrations of Ni–O–C bonds (Fig. 10c). This work showed direct findings to support that the dynamic formation of the C–C coupling (OC–COH) in the metal pair sites during CO_2 photoreduction reactions and the increased concentration of local *CO intermediates could effectively promote C–C coupling. Thus, the *in situ* spectroscopic measurements play an important role in revealing several key intermediates, such as *CO or *CHO.

Based on the accurate information of intermediates providing by *in situ* technologies, the prediction and screening of possible pathways among these intermediates can be complemented by density functional theory (DFT) calculations. With this strategy, Liu *et al.* calculated the Gibbs free energy and indicated that the energy barriers for the *CHO intermediate formation were 0.28 and −0.46 eV on carbon nitride before and after modification of amino-2-propanol, respectively,[67] suggesting the enhanced formation of *CHO with surface functionalization (Fig. 10d). Moreover, the formation Gibbs free energy of some key intermediates were also calculated to identify the optimal reaction pathways and to explain the high selectivity of the visible light-driven CO_2 conversion to CH_3CHO products. The results confirmed the C–C coupling to form CH_3CHO, and the multi-step hydrogenation process and reaction mechanism were then proposed (Fig. 10e).

The above four key aspects, including photocatalyst design, mass transfer control, determination of active sites, and reaction intermediate regulation need to be well considered to obtain multi-carbon products. First, an ideal photocatalyst design should allow to create abundant electrons with suppressed recombination of charges. Second, the increased mass transfer is to solve the slow kinetics of charges, and the elevated transfer benefits the multi-electron-coupled-proton-transfer process. Third, the active sites are designed to stabilize different intermediates of CO_2 and facilitate C–C coupling in photoreduction reactions. Last, the *in situ* spectroscopic measurements combining with DFT calculations assist to reveal the intermediates and potential reaction pathways.

5. Challenges and perspectives

In the past few decades, the design of photocatalyst has generally been the key focus in photocatalytic CO_2 reduction, and substantial developments have been demonstrated with different products. With continuous accumulation of new experimental and theoretical discoveries, there is no doubt that the understanding will continue to become deeper. However, we would like to emphasize the existing challenges in this field, as well as propose possible perspectives of photocatalytic conversion of CO_2 into long-chain hydrocarbons.

5.1 Challenges

(1) Limiting the competitive photocatalytic hydrogen evolution reaction (HER). The photocatalytic HER side reaction compete with CO_2 reduction for electrons and protons, and the overpotential of HER is typically lower than that of CO_2, especially for C_{2+} oxygenates. Thus, the critical challenge of inhibiting HER in this research area should be carefully understood and considered.

(2) Tracing the source of carbons in the products. Carbon source contamination is another key issue that needs special attention in the field of CO_2 photoreduction. The organic substances including solvents, reactants, and surfactants used for photocatalyst preparation may leave carbonaceous residues in the final products, and some of them may also decompose into small molecules such as CO and CH_4 during photocatalysis, resulting in overestimation of the photocatalytic activity.[111] Hence, more accurate and quantitative techniques are needed to confirm that the C1 products or C_{2+} oxygenates are originated from CO_2 molecules rather than other carbonaceous residues or contaminations.

(3) Although there have been a lot of topics on the photocatalytic reduction of CO_2 to C1 or C_{2+} oxygenates, it is still unclear how the local structure and coordination of the photocatalyst evolve during photoreduction process. To clarify this issue, the development of advanced characterizations with *in situ*, time-resolved, and elemental resolution spectroscopic technologies are necessary toward the exploration of reaction mechanisms.

5.2 Perspectives

At the end, we would also like to suggest the great opportunities of CO_2 upgrading into longer carbon chains, such as salicylic acid that is commonly used in fine chemicals, or polyethylene that is a basic unit of plastics. For example, salicylic acid is the main component of amoxicillin, which can be obtained by inserting CO_2 into the *ortho* position of phenol in the form of carboxyl groups.[112] Thus, converting CO_2 into fine chemicals or pharmaceutical intermediates may become one highly promising direction. To realize this goal, it is essential to make breakthroughs in the fabrication of high-efficiency photocatalysts with favorable stability. First, the fabrication of light-harvesting photocatalysts with appropriate band structures should be well designed, which can allow to utilize sufficient light energy to form more charge carriers. Second, the structure characteristics of photocatalysts need to be carefully comprehended, as the size of semiconductor crystals significantly affects the charge-transfer kinetics. Furthermore, the surface reaction kinetics, including interface CO_2 adsorption, intermediate formation, and product desorption, deserve deep investigation and understanding in CO_2 photoreduction reactions. Last, the rational design of cocatalysts to boost the reaction rates should be explored. In some cases, the design of

dual cocatalysts with tailored composition not only promotes charger separation, but also provides active sites to cooperate with the main photocatalysts to enhance the solar-driven CO_2 conversion. In summary, the CO_2 reduction products by photocatalysis will continue to evolve from C1 products to multicarbon oxygenates. In the near future, the transformation of CO_2 to even longer carbon-chain products with more complex structures will make breakthroughs in this highly exciting research field.

Conflicts of interest

The authors declare no conflict of interest.

Acknowledgements

We thank the following funding agencies for supporting this work: the National Key Research and Development Program of China (2018YFA0209401, 2017YFA0206901), the National Natural Science Foundation of China (22025502, 21975051), the Science and Technology Commission of Shanghai Municipality (21DZ1206800, 19XD1420400), and the Shanghai Municipal Education Commission (2019-01-07-00-07-E00045). Quan Zhang thanks the financial support from the China Postdoctoral Science Foundation (2022M710739).

Notes and references

1 J. Gowdy, *Futures*, 2020, **115**, 102488.
2 P. U. Clark, J. D. Shakun, S. A. Marcott, A. C. Mix, M. Eby, S. Kulp, A. Levermann, G. A. Milne, P. L. Pfister, B. D. Santer, D. P. Schrag, S. Solomon, T. F. Stocker, B. H. Strauss, A. J. Weaver, R. Winkelmann, D. Archer, E. Bard, A. Goldner, K. Lambeck, R. T. Pierrehumbert and G.-K. Plattner, *Nat. Clim. Change*, 2016, **6**, 360–369.
3 P. H. Soares, J. P. Monteiro, H. F. de Freitas, L. Ogiboski, F. S. Vieira and C. M. G. Andrade, *Atmosphere*, 2022, **13**, 358.
4 I. S. Omodolor, H. O. Otor, J. A. Andonegui, B. J. Allen and A. C. Alba-Rubio, *Ind. Eng. Chem. Res.*, 2020, **59**, 17612–17631.
5 S. Kar, A. Goeppert and G. K. S. Prakash, *Acc. Chem. Res.*, 2019, **52**, 2892–2903.
6 R. M. Cuéllar-Franca and A. Azapagic, *J. CO_2 Util.*, 2015, **9**, 82–102.
7 E. V. Kondratenko, G. Mul, J. Baltrusaitis, G. O. Larrazábal and J. Pérez-Ramírez, *Energy Environ. Sci.*, 2013, **6**, 3112–3135.
8 K. Li, B. Peng and T. Peng, *ACS Catal.*, 2016, **6**, 7485–7527.
9 H. Sun, C. Dong, A. Huang, H. Zhan, G. Wang, W. Liu, B. Ma and W. Wang, *Chem. – Eur. J.*, 2022, e202200019.
10 J. Fu, K. Jiang, X. Qiu, J. Yu and M. Liu, *Mater. Today*, 2020, **32**, 222–243.
11 X. Zhang, D. Xue, S. Jiang, H. Xia, Y. Yang, W. Yan, J. Hu and J. Zhang, *InfoMat*, 2022, **4**, e12257.
12 Y. Yang, Y. Tang, H. Jiang, Y. Chen, P. Wan, M. Fan, R. Zhang, S. Ullah, L. Pan, J.-J. Zou, M. Lao, W. Sun, C. Yang, G. Zheng, Q. Peng, T. Wang, Y. Luo, X. Sun, A. S. Konev, O. V. Levin, P. Lianos, H. Zhuofeng, Z. Shen, Q. Zhao, Y. Wang, N. Todorova, C. Trapalis, M. V. Sheridan, H. Wang, L. Zhang, S. Sun, W. Wang and J. Ma, *Chin. Chem. Lett.*, 2019, **30**, 2089–2109.
13 W. Ma, X. He, W. Wang, S. Xie, Q. Zhang and Y. Wang, *Chem. Soc. Rev.*, 2021, **50**, 12897–12914.
14 Y. Wang, D. Xu, X. Zhang, X. Hong and G. Liu, *Catal. Sci. Technol.*, 2022, **12**, 1539–1550.
15 J. Albero, Y. Peng and H. García, *ACS Catal.*, 2020, **10**, 5734–5749.
16 Y. Zhang, B. Xia, J. Ran, K. Davey and S. Qiao, *Adv. Energy Mater.*, 2020, **10**, 1903879.
17 W. Tu, Y. Zhou and Z. Zou, *Adv. Mater.*, 2014, **26**, 4607–4626.
18 Z. Zhang, G. Yi, P. Li, X. Zhang, H. Fan, X. Wang, C. Zhang and Y. Zhang, *Int. J. Energy Res.*, 2021, **45**, 9895–9913.
19 C. Xin, M. Hu, K. Wang and X. Wang, *Langmuir*, 2017, **33**, 6667–6676.
20 S. Tian, S. Chen, X. Ren, Y. Hu, H. Hu, J. Sun and F. Bai, *Nano Res.*, 2020, **13**, 2665–2672.
21 N.-N. Vu, S. Kaliaguine and T.-O. Do, *Adv. Funct. Mater.*, 2019, **29**, 1901825.
22 S. Wang, B. Y. Guan and X. W. Lou, *Energy Environ. Sci.*, 2018, **11**, 306–310.
23 Y. Zhou, Z. Wang, L. Huang, S. Zaman, K. Lei, T. Yue, Z. a. Li, B. You and B. Y. Xia, *Adv. Energy Mater.*, 2021, **11**, 2003159.
24 J. Z. Y. Tan, S. Gavrielides, H. R. Xu, W. A. Thompson and M. M. Maroto-Valer, *RSC Adv.*, 2020, **10**, 27989–27994.
25 H. Deng, F. Xu, B. Cheng, J. Yu and W. Ho, *Nanoscale*, 2020, **12**, 7206–7213.
26 Z. Miao, Q. Wang, Y. Zhang, L. Meng and X. Wang, *Appl. Catal., B*, 2022, **301**, 120802.
27 J. Ran, M. Jaroniec and S.-Z. Qiao, *Adv. Mater.*, 2018, **30**, 1704649.
28 T. Kong, Y. Jiang and Y. Xiong, *Chem. Soc. Rev.*, 2020, **49**, 6579–6591.
29 X. Chang, T. Wang and J. Gong, *Energy Environ. Sci.*, 2016, **9**, 2177–2196.
30 J. Mao, K. Li and T. Peng, *Catal. Sci. Technol.*, 2013, **3**, 2481–2498.
31 J. Li, H. Huang, W. Xue, K. Sun, X. Song, C. Wu, L. Nie, Y. Li, C. Liu, Y. Pan, H.-L. Jiang, D. Mei and C. Zhong, *Nat. Catal.*, 2021, **4**, 719–729.
32 Z. Chen, H. Zhang, P. Guo, J. Zhang, G. Tira, Y. J. Kim, Y. A. Wu, Y. Liu, J. Wen, T. Rajh, J. Niklas, O. G. Poluektov, P. D. Laible and E. A. Rozhkova, *J. Am. Chem. Soc.*, 2019, **141**, 11811–11815.
33 X. Xiong, C. Mao, Z. Yang, Q. Zhang, G. I. N. Waterhouse, L. Gu and T. Zhang, *Adv. Energy Mater.*, 2020, **10**, 2002928.
34 Y. A. Wu, I. McNulty, C. Liu, K. C. Lau, Q. Liu, A. P. Paulikas, C.-J. Sun, Z. Cai, J. R. Guest, Y. Ren,

V. Stamenkovic, L. A. Curtiss, Y. Liu and T. Rajh, *Nat. Energy*, 2019, **4**, 957–968.
35 H. Jun, S. Choi, M. Y. Yang and Y. S. Nam, *J. Mater. Chem. A*, 2019, **7**, 17254–17260.
36 J. Zhao, L. Xue, Z. Niu, L. Huang, Y. Hou, Z. Zhang, R. Yuan, Z. Ding, X. Fu, X. Lu and J. Long, *J. Power Sources*, 2021, **512**, 230532.
37 H. Zhang, J. Ming, J. Zhao, Q. Gu, C. Xu, Z. Ding, R. Yuan, Z. Zhang, H. Lin, X. Wang and J. Long, *Angew. Chem., Int. Ed.*, 2019, **58**, 7718–7722.
38 H. Zhang, P. Zhang, J. Zhao, Y. Liu, Y. Huang, H. Huang, C. Yang, Y. Zhao, K. Wu, X. Fu, S. Jin, Y. Hou, Z. Ding, R. Yuan, M. Roeffaers, S. Zhong and J. Long, *Angew. Chem., Int. Ed.*, 2021, **60**, 16009–16018.
39 J. Li, W. Cui, P. Chen, X. a. Dong, Y. Chu, J. Sheng, Y. Zhang, Z. Wang and F. Dong, *Appl. Catal., B*, 2020, **260**, 118130.
40 H. Dou, D. Long, X. Rao, Y. Zhang, Y. Qin, F. Pan and K. Wu, *ACS Sustainable Chem. Eng.*, 2019, **7**, 4456–4465.
41 Y. Diao, S. Jung, M. Kouhnavard, R. Woon, H. Yang, P. Biswas and J. M. D'Arcy, *ACS Cent. Sci.*, 2021, **7**, 1668–1675.
42 X. Li, Y. Sun, J. Xu, Y. Shao, J. Wu, X. Xu, Y. Pan, H. Ju, J. Zhu and Y. Xie, *Nat. Energy*, 2019, **4**, 690–699.
43 Y. Wang, R. Godin, J. R. Durrant and J. Tang, *Angew. Chem., Int. Ed.*, 2021, **60**, 20811–20816.
44 X. Meng, G. Zuo, P. Zong, H. Pang, J. Ren, X. Zeng, S. Liu, Y. Shen, W. Zhou and J. Ye, *Appl. Catal., B*, 2018, **237**, 68–73.
45 L. F. Garay-Rodríguez, L. M. Torres-Martínez and E. Moctezuma, *J. Photochem. Photobiol., A*, 2018, **361**, 25–33.
46 N. Li, B. Wang, Y. Si, F. Xue, J. Zhou, Y. Lu and M. Liu, *ACS Catal.*, 2019, **9**, 5590–5602.
47 T. Wang, L. Chen, C. Chen, M. Huang, Y. Huang, S. Liu and B. Li, *ACS Nano*, 2022, **16**, 2306–2318.
48 P.-H. Sung, C.-Y. Huang, C.-Y. Lin, P.-W. Chung, Y.-C. Chang, L.-C. Chen, H.-Y. Chen, C.-N. Liao, E.-L. Chiu and C.-Y. Wang, *J. CO_2 Util.*, 2022, **58**, 101920.
49 S. Sun, M. Watanabe, J. Wu, Q. An and T. Ishihara, *J. Am. Chem. Soc.*, 2018, **140**, 6474–6482.
50 F. Yu, X. Jing, Y. Wang, M. Sun and C. Duan, *Angew. Chem., Int. Ed.*, 2021, **60**, 24849–24853.
51 G. Wang, C.-T. He, R. Huang, J. Mao, D. Wang and Y. Li, *J. Am. Chem. Soc.*, 2020, **142**, 19339–19345.
52 Y. Wang, T. Ngoc Pham, Y. Tian, Y. Morikawa and L. Yan, *J. Colloid Interface Sci.*, 2021, **585**, 740–749.
53 G. Chen, R. Gao, Y. Zhao, Z. Li, G. I. N. Waterhouse, R. Shi, J. Zhao, M. Zhang, L. Shang, G. Sheng, X. Zhang, X. Wen, L.-Z. Wu, C.-H. Tung and T. Zhang, *Adv. Mater.*, 2018, **30**, 1704663.
54 J. Hao, D. Yang, J. Wu, B. Ni, L. Wei, Q. Xu, Y. Min and H. Li, *Chem. Eng. J.*, 2021, **423**, 130190.
55 W. Kim, T. Seok and W. Choi, *Energy Environ. Sci.*, 2012, **5**, 6066–6070.
56 Q. Chen, X. Chen, M. Fang, J. Chen, Y. Li, Z. Xie, Q. Kuang and L. Zheng, *J. Mater. Chem. A*, 2019, **7**, 1334–1340.
57 S. Sorcar, J. Thompson, Y. Hwang, Y. H. Park, T. Majima, C. A. Grimes, J. R. Durrant and S.-I. In, *Energy Environ. Sci.*, 2018, **11**, 3183–3193.
58 A. Gellé, T. Jin, L. de la Garza, G. D. Price, L. V. Besteiro and A. Moores, *Chem. Rev.*, 2020, **120**, 986–1041.
59 H. Park, H.-H. Ou, A. J. Colussi and M. R. Hoffmann, *J. Phys. Chem. A*, 2015, **119**, 4658–4666.
60 S. Yu, A. J. Wilson, J. Heo and P. K. Jain, *Nano Lett.*, 2018, **18**, 2189–2194.
61 J. Zhao, B. Liu, L. Meng, S. He, R. Yuan, Y. Hou, Z. Ding, H. Lin, Z. Zhang, X. Wang and J. Long, *Appl. Catal., B*, 2019, **256**, 117823.
62 X.-H. Xia, Z.-J. Jia, Y. Yu, Y. Liang, Z. Wang and L.-L. Ma, *Carbon*, 2007, **45**, 717–721.
63 C.-W. Lee, R. A. Kourounioti, J. C. S. Wu, E. Murchie, M. Maroto-Valer, O. E. Jensen, C.-W. Huang and A. Ruban, *J. CO_2 Util.*, 2014, **5**, 33–40.
64 Q. Han, Y. Zhou, L. Tang, P. Li, W. Tu, L. Li, H. Li and Z. Zou, *RSC Adv.*, 2016, **6**, 90792–90796.
65 I. Shown, H.-C. Hsu, Y.-C. Chang, C.-H. Lin, P. K. Roy, A. Ganguly, C.-H. Wang, J.-K. Chang, C.-I. Wu, L.-C. Chen and K.-H. Chen, *Nano Lett.*, 2014, **14**, 6097–6103.
66 L. Hurtado, R. Natividad and H. García, *Catal. Commun.*, 2016, **84**, 30–35.
67 Q. Liu, H. Cheng, T. Chen, T. W. B. Lo, Z. Xiang and F. Wang, *Energy Environ. Sci.*, 2022, **15**, 225–233.
68 T. Billo, F.-Y. Fu, P. Raghunath, I. Shown, W.-F. Chen, H.-T. Lien, T.-H. Shen, J.-F. Lee, T.-S. Chan, K.-Y. Huang, C.-I. Wu, M. C. Lin, J.-S. Hwang, C.-H. Lee, L.-C. Chen and K.-H. Chen, *Small*, 2018, **14**, 1702928.
69 Y. Yu, X. a. Dong, P. Chen, Q. Geng, H. Wang, J. Li, Y. Zhou and F. Dong, *ACS Nano*, 2021, **15**, 14453–14464.
70 A. Behera, A. K. Kar and R. Srivastava, *Mater. Horiz.*, 2022, **9**, 607–639.
71 H.-N. Wang, Y.-H. Zou, H.-X. Sun, Y. Chen, S.-L. Li and Y.-Q. Lan, *Coord. Chem. Rev.*, 2021, **438**, 213906.
72 S. C. Shit, I. Shown, R. Paul, K.-H. Chen, J. Mondal and L.-C. Chen, *Nanoscale*, 2020, **12**, 23301–23332.
73 S. Liu, B. Zhang, L. Zhang and J. Sun, *J. Energy Chem.*, 2022, **71**, 63–82.
74 S. Das, J. Pérez-Ramírez, J. Gong, N. Dewangan, K. Hidajat, B. Gates and S. Kawi, *Chem. Soc. Rev.*, 2020, **49**, 2937–3004.
75 F. Chen, T. Ma, T. Zhang, Y. Zhang and H. Huang, *Adv. Mater.*, 2021, **33**, 2005256.
76 M. Humayun, H. Ullah, L. Shu, X. Ao, A. Tahir, C. Wang and W. Luo, *Nano-Micro Lett.*, 2021, **13**, 209.
77 E. Karamian and S. Sharifnia, *J. CO_2 Util.*, 2016, **16**, 194–203.
78 N. W. Kinzel, C. Werlé and W. Leitner, *Angew. Chem., Int. Ed.*, 2021, **60**, 11628–11686.
79 L. Yuan, M.-Y. Qi, Z.-R. Tang and Y.-J. Xu, *Angew. Chem., Int. Ed.*, 2021, **60**, 21150–21172.

80 Q. Guo, F. Liang, X.-B. Li, Y.-J. Gao, M.-Y. Huang, Y. Wang, S.-G. Xia, X.-Y. Gao, Q.-C. Gan, Z.-S. Lin, C.-H. Tung and L.-Z. Wu, *Chem*, 2019, **5**, 2605–2616.
81 Y. Cao, X. He, N. Wang, H.-R. Li and L.-N. He, *Chin. J. Chem.*, 2018, **36**, 644–659.
82 C. Han, Y.-H. Li, J.-Y. Li, M.-Y. Qi, Z.-R. Tang and Y.-J. Xu, *Angew. Chem., Int. Ed.*, 2021, **60**, 7962–7970.
83 T. Baran, A. Dibenedetto, M. Aresta, K. Kruczała and W. Macyk, *ChemPlusChem*, 2014, **79**, 708–715.
84 Y. Yan, J. Chen, N. Li, J. Tian, K. Li, J. Jiang, J. Liu, Q. Tian and P. Chen, *ACS Nano*, 2018, **12**, 3523–3532.
85 Y. Wang, S. Wang and X. W. Lou, *Angew. Chem., Int. Ed.*, 2019, **58**, 17236–17240.
86 S. Han, B. Li, L. Huang, H. Xi, Z. Ding and J. Long, *Chin. J. Struct. Chem.*, 2022, **41**, 2201007–2201013.
87 Y. Liu, F. Yu, F. Wang, S. Bai and G. He, *Chin. J. Struct. Chem.*, 2022, **41**, 2201034–2201039.
88 B. Zhao, Y. Zhao, P. Liu, Y. Men, X. Meng and Y. Pan, *Chin. J. Struct. Chem.*, 2022, **41**, 2204012–2204021.
89 N. Li, X. Chen, J. Wang, X. Liang, L. Ma, X. Jing, D.-L. Chen and Z. Li, *ACS Nano*, 2022, **16**, 3332–3340.
90 X. Zhao, Y. Fan, W. Zhang, X. Zhang, D. Han, L. Niu and A. Ivaska, *ACS Catal.*, 2020, **10**, 6367–6376.
91 J. Di, C. Zhu, M. Ji, M. Duan, R. Long, C. Yan, K. Gu, J. Xiong, Y. She, J. Xia, H. Li and Z. Liu, *Angew. Chem., Int. Ed.*, 2018, **57**, 14847–14851.
92 X.-Y. Dong, Y.-N. Si, Q.-Y. Wang, S. Wang and S.-Q. Zang, *Adv. Mater.*, 2021, **33**, 2101568.
93 C. Gao, S. Chen, Y. Wang, J. Wang, X. Zheng, J. Zhu, L. Song, W. Zhang and Y. Xiong, *Adv. Mater.*, 2018, **30**, 1704624.
94 S. Ida, N. Kim, E. Ertekin, S. Takenaka and T. Ishihara, *J. Am. Chem. Soc.*, 2015, **137**, 239–244.
95 H. Huang, J. Zhao, B. Weng, F. Lai, M. Zhang, J. Hofkens, M. Roeffaers, J. Steele and J. Long, *Angew. Chem., Int. Ed.*, 2022, e202204563.
96 D. Giusi, C. Ampelli, C. Genovese, S. Perathoner and G. Centi, *Chem. Eng. J.*, 2021, **408**, 127250.
97 H. Huang, R. Shi, Z. Li, J. Zhao, C. Su and T. Zhang, *Angew. Chem., Int. Ed.*, 2022, **61**, e202200802.
98 A. Li, Q. Cao, G. Zhou, B. Schmidt, W. Zhu, X. Yuan, H. Huo, J. Gong and M. Antonietti, *Angew. Chem., Int. Ed.*, 2019, **58**, 14549–14555.
99 H. Zhou, J. Guo, P. Li, T. Fan, D. Zhang and J. Ye, *Sci. Rep.*, 2013, **3**, 1667.
100 S. Rej, M. Bisetto, A. Naldoni and P. Fornasiero, *J. Mater. Chem. A*, 2021, **9**, 5915–5951.
101 P. Li, L. Liu, W. An, H. Wang, H. Guo, Y. Liang and W. Cui, *Appl. Catal., B*, 2020, **266**, 118618.
102 X. Lin, S. Xia, L. Zhang, Y. Zhang, S. Sun, Y. Chen, S. Chen, B. Ding, J. Yu and J. Yan, *Adv. Mater.*, 2022, **34**, 2200756.
103 R. Das, S. Sarkar, R. Kumar, S. Ramarao, A. Jasil, C. Vinod, A. Singh and S. Peter, *ACS Catal.*, 2022, **12**, 687–697.
104 S. Xie, Y. Li, B. Sheng, W. Zhang, W. Wang, C. Chen, J. Li, H. Sheng and J. Zhao, *Appl. Catal., B*, 2022, **310**, 121320.
105 Y. Zhang, D. Yao, B. Xia, H. Xu, Y. Tang, K. Davey, J. Ran and S.-Z. Qiao, *Small Sci.*, 2021, **1**, 2000052.
106 B. Xia, Y. Zhang, J. Ran, M. Jaroniec and S.-Z. Qiao, *ACS Cent. Sci.*, 2021, **7**, 39–54.
107 Y. Hu, F. Zhan, Q. Wang, Y. Sun, C. Yu, X. Zhao, H. Wang, R. Long, G. Zhang, C. Gao, W. Zhang, J. Jiang, Y. Tao and Y. Xiong, *J. Am. Chem. Soc.*, 2020, **142**, 5618–5626.
108 J. Zhu, W. Shao, X. Li, X. Jiao, J. Zhu, Y. Sun and Y. Xie, *J. Am. Chem. Soc.*, 2021, **143**, 18233–18241.
109 S. Zhu, X. Li, X. Jiao, W. Shao, L. Li, X. Zu, J. Hu, J. Zhu, W. Yan, C. Wang, Y. Sun and Y. Xie, *Nano Lett.*, 2021, **21**, 2324–2331.
110 W. Shao, X. Li, J. Zhu, X. Zu, L. Liang, J. Hu, Y. Pan, J. Zhu, W. Yan, Y. Sun and Y. Xie, *Nano Res.*, 2022, **15**, 1882–1891.
111 Y. Zhang, D. Yao, B. Xia, M. Jaroniec, J. Ran and S.-Z. Qiao, *ACS Energy Lett.*, 2022, **7**, 1611–1617.
112 J. Luo, S. Preciado, P. Xie and I. Larrosa, *Chem. – Eur. J.*, 2016, **22**, 6798–6802.